공학석사학위논문

Waveform inversion for deep sea seismic data with limited-offset condition

- Application to Sumatra WG2 line field data -

제한된 오프셋의 심해 탐사자료에 대한 파형역산

2013년 2월

서울대학교 대학원
에너지시스템공학부
조 용 채

Waveform inversion for deep sea seismic data with limited-offset condition

- Application to Sumatra WG2 line field data -

제한된 오프셋의 심해 탐사자료에 대한 파형역산

지도교수 신 창 수

이 논문을 공학석사 학위논문으로 제출함.
2012년 12월

서울대학교 대학원
에너지시스템공학부
조 용 채

조 용 채의 공학석사 학위논문을 인준함.
2013년 1월

위 원 장 _____ (인)

부위원장 _____ (인)

위 원 _____ (인)

Abstract

Waveform inversion for deep sea seismic data with limited-offset condition
- Application to Sumatra WG2 line field data -

Yongchae Cho
Department of Energy systems Engineering
Seoul National University

To alleviate the drawbacks of conventional frequency-domain inversion such as local minima or sensitivity to noise, Laplace-Fourier-domain full waveform inversion is considered one of the most reliable schemes for constructing a velocity model. By using a damped wavefield, we can reduce the possibility of converging to local minima to produce an accurate long-wavelength velocity model. Then, we can obtain final inversion results using high-frequency components and low damping coefficients. However, the imaging area is limited because this scheme uses a damped wavefield that makes the magnitudes of the gradient and residual small in deep water. Generally, the imaging depth of a Laplace-Fourier inversion is less than the half the streamer length. Thus, dealing with seismic data in the deep-sea layer is difficult. The deep-sea layer reduces the amplitude of signals and acts as an obstacle to computing an exact gradient image. To reduce the water layer effect, we extrapolated the wavefield with a downward continuation and performed refraction tomography. Then,

we performed a Laplace-Fourier-domain inversion using refraction tomography results as an initial model. After obtaining a final velocity model, we verified the inversion results using reverse-time migration. We applied this method to both synthetic (Marmousi) and field (Sumatra WG2 line) data. Through the test, we concluded that despite a relatively short streamer length compared to the water depth, the Laplace-Fourier inversion with refraction tomography of the downward-continued wavefield recovers the subsurface structure located below the conventional imaging depth.

Keywords : Laplace-Fourier domain inversion, Downward continuation, Refraction tomography, Deep-sea seismicdata

Student Number : 2011-21111

Contents

List of Figures

List of Tables

Chapter 1

Introduction

When performing prestack depth migration, we must construct exact subsurface structures for the migration image with high resolution. A variety of research has been conducted to develop velocity-building schemes such as inversion or reflection tomography. Reflection tomography [Murphy et al., 1999[26]; Zang et al., 1998[41]; Chiu et al., 1986[4]] has been the method of choice for recovering subsurface velocity structures since the introduction of the method using the travel-time of seismic reflection [Bishop, 1984[2]]. However, reflection tomography requires the reflectors to be defined through interpretation. Defining the exact reflection boundary is difficult and requires a great deal of time. In addition, if the defined geological structure is incorrect, we cannot expect to obtain a reliable velocity model. As an alternative to tomography, a full-waveform inversion scheme was introduced using the difference between the simulated data and the field data to recover the subsurface parameters. This idea has been greatly advanced by the development of the back-propagation algorithm [Lailly, 1983[21]; Tarantola, 1984[39]]. The conventional full-waveform inversion, however, has several weaknesses in recovering the field data such as the local minimum problem [Mora, 1987[25]], an absence of low-frequency components, and an inability to handle field data that contain noise. Increasing the offset during acquisition could be considered as an alternative because we can obtain long-wavelength signals through

acquisition using a wide azimuth. A long-wavelength signal is important for building a macro velocity model. However, increasing the offset is expensive, and gaining a low-frequency signal from short-offset field data is difficult due to technical limitations [Symes, 2008[38]].

Shin and Cha [2008[32]] suggested a Laplace-domain full-waveform inversion using a damped wavefield to overcome the conventional limitations. The use of a damped wavefield eliminates the concern regarding the absence of a low-frequency signal. After multiplying the damping function over the field data, certain regions of the frequency are altered to a signal with low frequency allowing us to obtain a long-wavelength signal from field data that have few or no long-wavelength components. Thus, despite the previously mentioned limitations, Laplace-domain inversion can recover the macro velocity structure of field data [Shin and Ha, 2008[34]]. Laplace-domain inversion is sensitive to the noise that is presented around the first-break signal; therefore, one must eliminate the noise that occurs early in the shot gather through muting [Shin and Cha, 2008[32]; Ha et al., 2010[16]]. After acquiring a macro-velocity model through Laplace-domain inversion, we can recover the high-resolution velocity model by combining it with the conventional frequency-domain inversion called Laplace-Fourier inversion [Shin and Cha, 2009[33]; Shin et al., 2010[35]]. This scheme is similar to the method in which a long-wavelength velocity model is first constructed; then, a short-wavelength component is used to recover the velocity structure as suggested by Pratt et al. [1998[28]].

Laplace- and Laplace-Fourier-domain inversions are able to deal with seismic data that are properly offset when compared with the water depth. However, in the case of field data with a deep-sea layer, we cannot expect to recover

the exact subsurface structure. In the field of petroleum engineering, deep sea is defined as the sea water deeper than 1 km. Similary, in geophysics field, it is defined as sea water that is deeper than 2 km. When we deal with deep sea seismic data with Laplace-Fourier inversion, after applying a damping function, the amplitude of the signal propagating through the deep area decreases, which hinders the accurate computation of a gradient image. For this reason, the imaging depth of Laplace-Fourier inversion is generally less than the half the streamer length. In this study, to reduce the water layer effect, we applied an extrapolated wavefield with a downward continuation to the field data. This process makes the interpretation and construction of a macro-velocity model through refraction tomography easier. Once the macro-velocity model with downward-continued data was built, we performed Laplace-Fourier inversion to recover a more accurate velocity image by applying high-frequency signals. To prove the reliability of the inversion results, we performed reverse-time migration based on the velocity model obtained through inversion.

In Chapter 2 of this paper, we will discuss the theory of Laplace-Fourier inversion, downward continuation, and tomography. We applied this scheme to both simulated and field data. The results and related explanation are presented in Chapters 3 and 4, which provide the results of simulated and field data, respectively. In the final chapter, we presented a brief comparison of the results and our expectations for development in this area.

Chapter 2

Theory

2.1 Laplace-Fourier full waveform inversion

2.1.1 Relationship beween Fourier- & Laplace-domain

No obvious relationship exists between the Fourier and Laplace domains without profound mathematical insight. However, the relationship of the two transformed methods is easily explained through the generalized Laplace transform, which can be given by

$$\tilde{u}(s) = \int_0^\infty u(t)e^{-st}dt, \tag{2.1}$$

where s is the damping coefficient in the Laplace domain. Generally, a Fourier transform is a function of the real variable, the so-called angular frequency ω, and the Laplace transform is a function of the complex variable s. If s is substituted with $s = s_r - i\omega$, then equation 2.1 becomes

$$\tilde{u}(s_r - i\omega) = \int_{-\infty}^\infty u(t)e^{i(\omega + is_r)}dt. \tag{2.2}$$

Equation 2.2 represents the generalized Laplace transform expressed using the terms of the Fourier transform with complex variables. If we set the real portion of the term ω to zero, the format of equation 2.2 will match that of the Laplace transform. Thus, we can explain that the Laplace-domain inversion

is a conventional inversion with a zero-frequency component. In the Laplace-Fourier-domain inversion, we can control the frequency loop composed of (ω, s) to determine the exact global solution. The type of frequency loops can be set sequentially as suggested by Shin et al. [2010[35]] or combined into several groups.

2.1.2 Objective function

The basic concept of inversion involves reducing the residual between measured data (u_{ij}) and modeled data (d_{ij}) using an objective function. Setting an objective function is a first step in constructing an inversion algorithm. In the objective function, we must define the type of residual; the residual refers to the difference between the observed wavefields and modeled wavefields. An algorithm's sensitivity to noise is dependent on the type of objective function. Thus, the choice of objective function is important to a given inversion scheme. Claerbout and Muir [1973[8]] and Pyun et al. [2009[30]] suggested the l_1-norm objective function, which can apparently handle noise with a strong amplitude. Amundsen [1991[1]] suggested the Cauchy function, which is resistant to random noise. Bube and Langean [1997[3]] and Ha et al. [2009[14]] suggested the Huber function, which selects the l_1 and l_2 norm according to the magnitude of the residual. One of the most widely used objective functions is the l_2 norm that can be written as follows (2.3):

$$E = \frac{1}{2}\sum_{i=1}^{N_s}\sum_{j=1}^{N_r}(u_{ij} - d_{ij})^2 \tag{2.3}$$

where N_s and N_r represent the number of the source and receiver, respectively. The value u_{ij} is the modeled wavefield, and d_{ij} represents the observed data. However, its sensitivity to noise and the high nonlinearity of the wave equations make this function impractical for applications in the area of inversion [Jannane et al., 1989[19]]. Therefore, we will perform a full-waveform inversion, not in a time or frequency domain but in the Laplace or Laplace-Fourier domain. The Laplace domain has distinctive features compare with the conventional domain, such as time or frequency. In a Laplace-domain inversion, we use a damped wavefield. After damping, the signal around the source is dominant compared with the large-offset signals. Thus, the signal propagated from a deeper portion of the subsurface can be ignored because of its weak amplitude. Thus, Green's function exhibits singularity around the source position. Except for the source position, the magnitude of the wavefield is small making it difficult to compute the exact residual. Therefore, to improve the resolution of the Laplace inversion results, we adopted the logarithmic objective function suggested by Shin and Min [2006[36]]. The form of the function can be presented as follows:

$$E = \frac{1}{2}\sum_{i=1}^{N_s}\sum_{j=1}^{N_r}\left(\ln\frac{|\tilde{u}_{ij}|}{|\tilde{d}_{ij}|}\right)^2 \tag{2.4}$$

where N_s, N_r are the number of the source and receiver, respectively; $\tilde{u}_{ij}$ and $\tilde{d}_{ij}$ represent the Laplace-transformations of modeled and observed wavefields.

2.1.3 The gradient of objective function

The logarithmic objective function at a certain angular frequency (ω) can be presented as follows:

$$E(\mathbf{p}) = \frac{1}{2}\sum_{i=1}^{N_s}\sum_{j=1}^{N_r}\left(\ln\frac{|\tilde{u}_{ij}|}{|\tilde{d}_{ij}|}\right)\left(\ln\frac{|\tilde{u}_{ij}|}{|\tilde{d}_{ij}|}\right)^{*} \tag{2.5}$$

where $\mathbf{p}$ is the model parameter, $\tilde{u}_{ij}$ represents the modeled wavefields and $\tilde{d}_{ij}$ is the Laplace-Fourier-transformed data. The asterisk (*) denotes a complex conjugate. The term $\ln\frac{|\tilde{u}_{ij}|}{|\tilde{d}_{ij}|}$ is termed the residual $\mathbf{r}$, and our aim is to set the direction of the gradient to reduce the residual. By taking the partial derivative of equation 2.5, the steepest descent direction can be obtained as follows:

$$\frac{\partial E(\mathbf{p})}{\partial p_k} = \mathbf{Re}\left[\sum_{i=1}^{N_s}\sum_{i=1}^{N_s}\frac{1}{\tilde{u}_{ij}}\frac{\partial\tilde{u}_{ij}}{\partial p_k}\left(\ln\frac{|\tilde{u}_{ij}|}{|\tilde{d}_{ij}|}\right)^{*}\right]. \tag{2.6}$$

By considering all the model parameters, equation 2.6 can be rewritten in matrix form:

$$\begin{bmatrix} \frac{\partial E}{\partial p_1} \\ \frac{\partial E}{\partial p_2} \\ \frac{\partial E}{\partial p_3} \\ \vdots \\ \frac{\partial E}{\partial p_{m-1}} \\ \frac{\partial E}{\partial p_m} \end{bmatrix} = \mathbf{Re}\begin{bmatrix} \frac{\partial\tilde{u}_1}{\partial p_1} & \frac{\partial\tilde{u}_2}{\partial p_1} & \cdots & \frac{\partial\tilde{u}_{n-1}}{\partial p_1} & \frac{\partial\tilde{u}_n}{\partial p_1} \\ \frac{\partial\tilde{u}_1}{\partial p_2} & \frac{\partial\tilde{u}_2}{\partial p_2} & \cdots & \frac{\partial\tilde{u}_{n-1}}{\partial p_2} & \frac{\partial\tilde{u}_n}{\partial p_2} \\ \frac{\partial\tilde{u}_1}{\partial p_3} & \frac{\partial\tilde{u}_2}{\partial p_3} & \cdots & \frac{\partial\tilde{u}_{n-1}}{\partial p_3} & \frac{\partial\tilde{u}_n}{\partial p_3} \\ \vdots & \vdots & \ddots & \vdots & \vdots \\ \frac{\partial\tilde{u}_1}{\partial p_{m-1}} & \frac{\partial\tilde{u}_2}{\partial p_{m-1}} & \cdots & \frac{\partial\tilde{u}_{n-1}}{\partial p_{m-1}} & \frac{\partial\tilde{u}_n}{\partial p_{m-1}} \\ \frac{\partial\tilde{u}_1}{\partial p_m} & \frac{\partial\tilde{u}_2}{\partial p_m} & \cdots & \frac{\partial\tilde{u}_{n-1}}{\partial p_m} & \frac{\partial\tilde{u}_n}{\partial p_m} \end{bmatrix}\begin{bmatrix} \frac{1}{\tilde{u}_1}\ln\frac{\tilde{u}_1}{\tilde{d}_1} \\ \vdots \\ \frac{1}{\tilde{u}_{N_r}}\ln\frac{\tilde{u}_{N_r}}{\tilde{d}_{N_r}} \\ 0 \\ \vdots \\ 0 \end{bmatrix}, \tag{2.7}$$

where, m indicates the number of parameters, and N_r represents the number of receivers on the surface. To calculate the partial derivative wavefields, we

used the differentiating form of the frequency-domain wave equation $\mathbf{Su} = \mathbf{f}$ [Marfurt, 1984[22]]. Taking the partial differential of this equation with respect to a model parameter p_k yields the following:

$$\frac{\partial \mathbf{S}}{\partial p_k}\tilde{\mathbf{u}} + \mathbf{S}\frac{\partial \tilde{\mathbf{u}}}{\partial p_k} = 0, \quad (k = 1,2,\ldots,m) \tag{2.8}$$

or

$$\frac{\partial \tilde{\mathbf{u}}}{\partial p_k} = \mathbf{S}^{-1}\mathbf{v}_k, \quad (k = 1,2,\ldots,m) \tag{2.9}$$

where, m is the number of parameters, and

$$\mathbf{v}_k = -\frac{\partial \mathbf{S}}{\partial p_k}\tilde{\mathbf{u}}. \quad (k = 1,2,\ldots,m) \tag{2.10}$$

In equation 2.10, $\mathbf{v}_k$ is the virtual source vector required to perturb the l^{th} parameter of the element [Pratt et al, 1998[29]]. To obtain the partial derivative, the Jacobian J $\left(\frac{\partial \tilde{\mathbf{u}}}{\partial p_k}\right)$ shown in equation 2.7, we can use the form provided in equation 2.9. The partial derivative wavefields are composed of a convolution between Green's function and the virtual source vector. By substituting equation 2.9 into equation 2.6, we can obtain the gradient of the objective function as follows:

$$\frac{\partial E(\mathbf{p})}{\partial p_k} = \mathbf{Re}\left[(\mathbf{S}^{-1}\mathbf{v}_k)^T\mathbf{r}\right], \tag{2.11}$$

where

$$\mathbf{r} = \left[\frac{1}{\tilde{u}_1}\ln\frac{\tilde{u}_1}{\tilde{d}_1} \quad \frac{1}{\tilde{u}_2}\ln\frac{\tilde{u}_2}{\tilde{d}_2} \quad \ldots \quad \frac{1}{\tilde{u}_{N_r}}\ln\frac{\tilde{u}_{N_r}}{\tilde{d}_{N_r}} \quad 0 \quad \ldots \quad 0\right]^T. \tag{2.12}$$

In equation 2.12, N_r represents the number of receivers. The impedance matrix $\mathbf{S}$ has a symmetric form and satisfies the reciprocity condition. Thus, we can

modify equation 2.6 as follows:

$$\frac{\partial E(\mathbf{p})}{\partial p_k} = \mathbf{Re}\left[(\mathbf{v}_k)^T \mathbf{S}^{-1}\mathbf{r}\right], \tag{2.13}$$

Consequently, using the steepest descent method, the gradient of the objective function E can be computed by determining the zero-lag convolution between the back-propagated residual data in a time-reversed order using a two-way wave equation and the virtual source vector [Plessix, 2006[27]].

2.1.4 The construction of Hessian matrix

In the steepest descent method, we have to construct the Hessian matrix to obtain a global minimum. The Hessian matrix acts as a scale factor for the gradient vector and enhances the resolution of the deeper region of the geological model. To obtain the final form of the parameter updating equation, we must begin with the objective function expanded in terms of the subsurface parameter ($\mathbf{p}$) as follows:

$$E(\mathbf{p}+\Delta\mathbf{p}) = E(\mathbf{p}) + \nabla_{\mathbf{p}} E(\mathbf{p})\Delta p + \frac{1}{2}\nabla_{\mathbf{p}}\mathbf{H}\Delta\mathbf{p} + \mathbf{O}\left(|\Delta p|^3\right) \tag{2.14}$$

where, $\mathbf{H}$ can be written as

$$H_{ij} = \frac{\partial^2 E\mathbf{p}}{\partial p_i \partial p_j}, \quad i = 1,2,\ldots,m, \quad j = 1,2,\ldots m. \tag{2.15}$$

After ignoring the error terms as shown in equation 2.14, we can obtain the simplified parameter by updating the equation as follows:

$$\mathbf{p}_{k+1} = \mathbf{p}_k - \mathbf{H}^{-1}\Delta_{\mathbf{p}}E(\mathbf{p}) \tag{2.16}$$

The use of the complete equation 2.15 for the Hessian matrix requires extensive computer capacity and time. The Hessian matrix for the iterative solution named the full-Newton method can be written as follows:

$$\begin{aligned} H_{ij} &= \frac{\partial}{\partial p_i}\left(\frac{\partial E}{\partial p_j}\right) \\ &= \frac{\partial}{\partial p_i}\mathbf{Re}\left[\left(\frac{\partial u}{\partial p_i}\right)^T \mathbf{r}^*\right] \\ &= \mathbf{Re}\left[\left(\frac{\partial u}{\partial p_i}\right)^T \left(\frac{\partial u}{\partial p_i}\right)^* + \frac{\partial^2 u}{\partial p_i \partial p_j}\mathbf{r}^*\right]. \end{aligned} \tag{2.17}$$

Equation 2.17 can be rewritten in matrix form as:

$$H_{ij} = \mathbf{Re}\left\{ \begin{bmatrix} \frac{\partial u_1}{\partial p_i} & \cdots & \frac{\partial u_n}{\partial p_i} \end{bmatrix} \begin{bmatrix} \frac{\partial u_1^*}{\partial p_j} \\ \frac{\partial u_1^*}{\partial p_j} \\ \vdots \\ \frac{\partial u_1^*}{\partial p_j} \end{bmatrix} + \begin{bmatrix} \frac{\partial^2 u_1}{\partial p_i \partial p_j} & \cdots & \frac{\partial^2 u_n}{\partial p_i \partial p_j} \end{bmatrix} \begin{bmatrix} r_1^* \\ r_1 \\ \vdots \\ r_1 \end{bmatrix} \right\} \tag{2.18}$$

The equation 2.18 can be simplified as follows,

$$\begin{aligned} H_{ij} &= \mathbf{Re}\left\{\mathbf{J}^T\mathbf{J}^*\right\} + \mathbf{Re}\left\{\left[\left(\frac{\partial}{\partial p_1}\mathbf{J}^T\right)\mathbf{r}^* \quad \cdots \quad \left(\frac{\partial}{\partial p_m}\mathbf{J}^T\right)\mathbf{r}^*\right]\right\} \\ &= \mathbf{H}_\alpha + \mathbf{R} \end{aligned} \tag{2.19}$$

As previously stated, using the complete function requires too much time and computing resources. To solve this problem, we can ignore the $\mathbf{R}$ term in equation 2.20. This method that considers only the $\mathbf{J}^T\mathbf{J}^*$ components is called

the Gauss-Newton method. However, this scheme also requires a great deal of computer memory. We can enhance the efficiency by considering only the diagonal components of the pseudo-Hessian matrix. The pseudo-Hessian of the logarithmic objective function used in this study was obtained from Ha et al [2012[15]]. The derivation of the pseudo-Hessian begins with an approximated Hessian:

$$\begin{aligned} H_{ij} &= \mathbf{Re}\left\{\mathbf{J}^T\mathbf{J}^*\right\} \\ &= \mathbf{Re}\begin{bmatrix}\mathbf{v}_{(1)}^T & \cdots & \mathbf{v}_{(m)}^T\end{bmatrix}(\mathbf{S}^{-1})^T(\mathbf{S}^{-1})\begin{bmatrix}\mathbf{v}_{(1)}^* & \cdots & \mathbf{v}_{(m)}^*\end{bmatrix}, \end{aligned} \tag{2.20}$$

in which $\mathbf{v}_k$ denotes the virtual source, and the multiplication of the Green's function term $(\mathbf{S}^{-1})^T\mathbf{S}^{-1}$ can be approximated by the identity matrix $\mathbf{I}$. The matrix form of the equation 2.20 is as follows:

$$H_{ij} = \mathbf{Re}\begin{bmatrix} \mathbf{v}_{(1)}^T\mathbf{v}_{(1)}^* & \mathbf{v}_{(2)}^T\mathbf{v}_{(1)}^* & \cdots & \mathbf{v}_{(m)}^T\mathbf{v}_{(1)}^* \\ \mathbf{v}_{(1)}^T\mathbf{v}_{(2)}^* & \mathbf{v}_{(2)}^T\mathbf{v}_{(2)}^* & \cdots & \mathbf{v}_{(m)}^T\mathbf{v}_{(2)}^* \\ \vdots & \vdots & \ddots & \vdots \\ \mathbf{v}_{(1)}^T\mathbf{v}_{(m)}^* & \mathbf{v}_{(2)}^T\mathbf{v}_{(m)}^* & \cdots & \mathbf{v}_{(m)}^T\mathbf{v}_{(m)}^* \end{bmatrix}. \tag{2.21}$$

Selecting the diagonal components from the approximated Hessian yields the pseudo-Hessian matrix:

$$diag\mathbf{H}_p = \begin{bmatrix}\mathbf{v}_{(1)}^T\mathbf{v}_{(1)}^* & \mathbf{v}_{(2)}^T\mathbf{v}_{(2)}^* & \cdots & \mathbf{v}_{(m)}^T\mathbf{v}_{(m)}^*\end{bmatrix}. \tag{2.22}$$

Applying this form of the matrix to the inversion scheme requires a stabilizing factor λ due to the singularity of the pseudo-Hessian matrix. By adding the terms on $diag\mathbf{H}_p$, we can, on average, rescale the magnitude of each term.

We can obtain higher resolution by controlling this λ term. If we set a lower value for λ, the imaging depth will increase over that of a high λ value, which can image only a shallow area of the subsurface. However, through many tests using a variety of λ values, we found 10^{-6} to be generally appropriate. Substituting the updated step length α, the gradient of the objective function, and equation 2.16 into equation 2.22 yields the k^{th} node of the updated equation as follows:

$$\begin{aligned}\mathbf{p}_{k+1} &= \mathbf{p}_k - \alpha(diag\mathbf{H}_p + \lambda\mathbf{I})^{-1}\nabla_{\mathbf{p}}E(\mathbf{p}) \\ &= \mathbf{p}_k - \alpha\sum_{i=1}^{N_f}\frac{\sum_{j=1}^{N_s}\mathbf{Re}\left[(\mathbf{v}_l)^T\mathbf{S}^{-1}\mathbf{r}\right]}{\sum_{j=1}^{N_s}\mathbf{Re}\left[(\mathbf{v}_l)^T(\mathbf{v}_l)^*\right]+\lambda}.\end{aligned} \tag{2.23}$$

Based on equation 2.23, we can design the algorithm of the Laplace-Fourier inversion as shown in Figure 2.1.

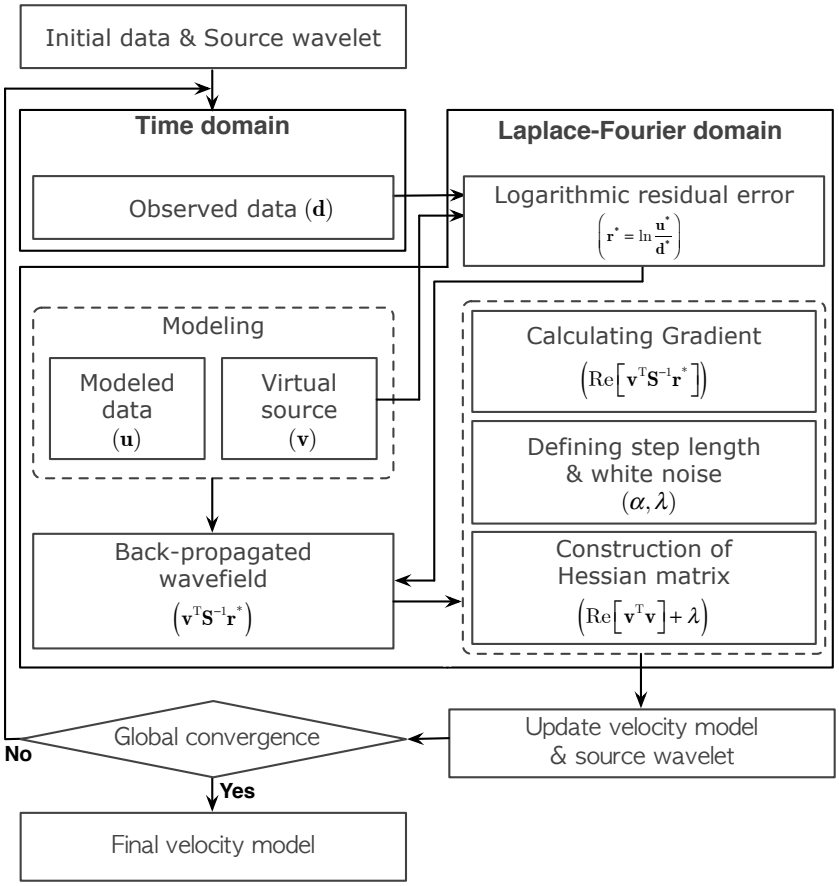

Figure 2.1: Workflow of Laplace-Fourier inversion.

2.1.5 Source estimation for the logarithmic function

When we consider synthetic data, we obtain information regarding the exact source wavelet. However, obtaining information on the exact source proves difficult in field data. In addition, to reduce the differences between the modeled wavefield and the observed data, one must recover an accurate source wavelet. Shin and Min [2006[36]] demonstrated that a source wavelet can be estimated by separating the amplitude and the phase of a complex source function. The objective function for the source wavelet can be presented as follows:

$$E = \frac{1}{2}\sum_{i=1}^{N_s}\sum_{i=1}^{N_s}\left[\left\{\ln\left(\frac{A^{src}A_{ij}^{G}}{A_{ij}^{d}}\right)\right\}^2 + \left(\theta^{src}+\theta_{ij}^{G}-\theta_{ij}^{d}\right)\right], \tag{2.24}$$

in which N_s and N_r are the total number of shots and receivers, respectively. The values A and θ represent the amplitude and phase. The superscripts *src*, G, and d denote the source wavelet, Green's function and the observed data, respectively. Hence, the modeled data and the observed data can be written as follows:

$$u_{ij} = A^{src}A_{ij}^{G}e^{i\left(\theta^{src}+\theta_{ij}^{G}\right)}, \quad d_{ij} = A_{ij}^{d}e^{i\theta_{ij}^{d}} \tag{2.25}$$

If we set the logarithmic amplitude of the source wavelet to $z = \ln A^{src}$, the gradient and the Hessian of the objective function to recover the amplitude of the source are expressed as follows:

$$\frac{\partial E}{\partial z} = \sum_{i=1}^{N_s}\sum_{j=1}^{N_r}\mathbf{Re}\left[z+\ln\frac{A_{ij}^{G}}{A_{ij}^{d}}\right], \tag{2.26}$$

and

$$\frac{\partial^2 E}{\partial^2 z} = \sum_{i=1}^{N_s} \sum_{j=1}^{N_r} 1, \tag{2.27}$$

respectively. We can estimate the amplitude of the source wavelet by updating it through several iterations as follows:

$$z(k+1) = z(k) - \frac{\sum_{i=1}^{N_s} \sum_{j=1}^{N_r} \mathbf{Re}\left[z + \ln \frac{A_{ij}^G}{A_{ij}^d}\right]}{\sum_{i=1}^{N_s} \sum_{j=1}^{N_r} 1}, \tag{2.28}$$

where k is the iteration count.

2.2 Refraction tomography with extrapolated wavefield

2.2.1 Downward continuation

When we deal with seismic data in the deep-sea layer, the first break signal appears later and most of the signals are composed of reflections that are not combined with refraction. If acquisition is performed using a much longer streamer than the depth of the sea layer, the deep-water layer will not act as an obstacle to imaging the subsurface. However, using long streamer is quite expensive. Thus, removing the effect through a computational approach in data processing would greatly reduce the research budget. In this study, we eliminated the effect of water by extrapolating the wavefield using the downward continuation method. Downward continuation can be performed in several ways: the Kirchhoff integral or a prestack phase-shift scheme, the finite difference solution of the wave equation and as in this study, an approach with a prestack phase-shift. The principal objective of downward continuation is to transform the seismic wavefield $u(x_s, x_r, t, z_0)$ to the wavefield $u(x_s', x_r', t', z_0)$ at a depth z in which z_0 indicates the location of the sea surface and z indicates the depth of the shots and the receiver location following downward continuation. The x_s and x_r terms are source and receiver positions, respectively. The term t indicates the travel time of the wavefield. After a double Fourier transform, the wavefield of the sea surface can be written as $u(k_{xs}, k_{xr}, \omega, z_0)$, with the horizontal and vertical wave numbers k_x, k_z, and the angular frequency component ω, respectively. By snell's law, slowness can be rewritten in terms of k and ω as follows:

$$\begin{aligned}\frac{k_x}{\omega} &= \frac{\partial t_0}{\partial x} = \frac{\sin\theta}{v} = p,\\ \frac{k_z}{\omega} &= \frac{\partial t_0}{\partial z} = \frac{\cos\theta}{v} = \frac{\sqrt{1-p^2v^2}}{v}\end{aligned} \tag{2.29}$$

The wavenumber terms can be calculated using a 2-D dispersion relationship $k_x^2 + k_z^2 = \omega^2/c^2$, the horizontal slowness number (p) or the incident angle (θ) as follows:

$$k_x = \omega p, \quad k_z = \sqrt{\frac{\omega^2}{c^2} - k_x^2} \tag{2.30}$$

based on the horizontal slowness relation $p = \frac{\sin\theta}{c}$ and the trigonometric function relations $\sin\theta = \frac{ck_x}{\omega}$ and $\cos\theta = \frac{ck_z}{\omega}$. By applying time and distance shifts for the source $(\tau_s, \Delta x_s)$ and the receivers $(\tau_r, \Delta x_r)$, the wavefield following the downward continuation can be expressed as

$$u(k_{xs}, k_{xr}, \omega, z) = u(k_{xs}, k_{xr}, \omega, z_0)\, e^{[i(\tau_s + \tau_r + \Delta x_s + \Delta x_r)]} \tag{2.31}$$

where, $\tau_s = k_{zs}z$ and $\tau_r = k_{zr}z$, $\Delta x_s = \frac{k_{xs}}{k_{zs}}z$ and $\Delta x_r = -\frac{k_{xr}}{k_{zr}}z$, respectively. At last, we can obtain the seismic wavefield $u(x_s', x_r', t', z)$ of time-distance domain by using double inverse Fourier transform of wavenumber (k_x,k_z) and angular frequency (ω). $\tau_s = k_{zs}z$ and $\tau_r = k_{zr}z$, $\Delta x_s = \frac{k_{xs}}{k_{zs}}z$ and $\Delta x_r = -\frac{k_{xr}}{k_{zr}}z$. Finally, we can obtain the seismic wavefield $u(x_s', x_r', t', z)$ of the time-distance domain using the double inverse Fourier transform of the wavenumber (k_x,k_z) and the angular frequency (ω). Figure 2.2 presents the impact of downward continuing a 12.0-km-long streamer shot record from a WG2 profile to obtain source and receiver positions on the sea floor [Martin et al., 2012[23]]. As shown in Figure

2.2, the direct-wave signals and the sea floor reflections disappear, and the region of refraction is enhanced. After applying a downward continuation, the reflection signals are distorted and the ability to use complete signals in several imaging schemes, such as the frequency-domain full-waveform inversion, is limited. In addition, we cannot use both sides of the seismic data because of the unstable results that arise with downward continuation. During the extrapolation process, neither side coincident with the streamer length contains the complete ray path components. Therefore, our use of some portions of the seismic data is limited. However, this idea has strong merits. The downward-continued data are much easier to interpret and useful for constructing the macro-velocity model through refraction tomography.

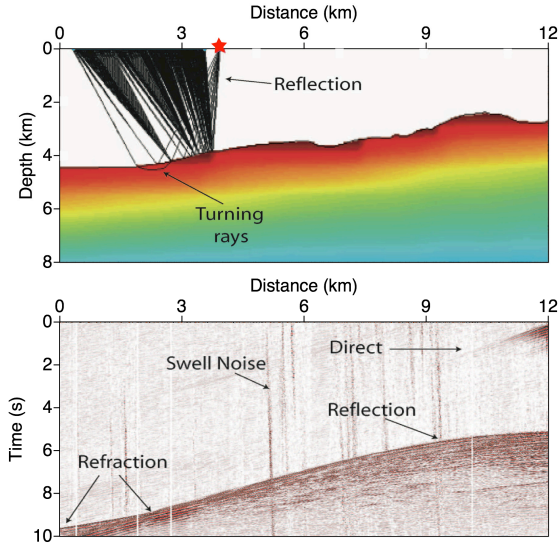

(a)

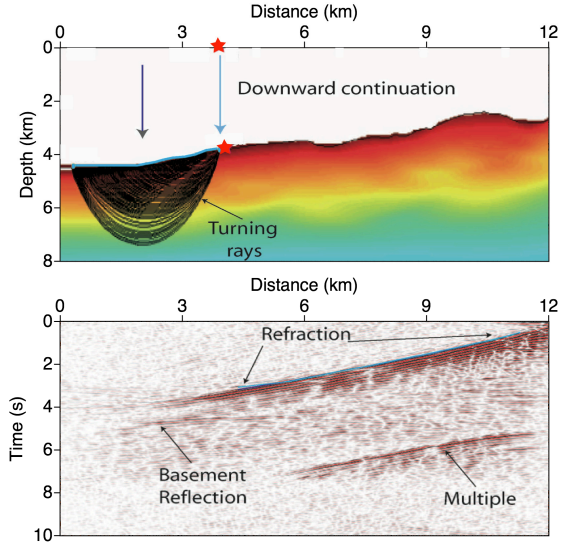

(b)

Figure 2.2: Downward-continued shot gather. The Sumatra dataset WG2 was used for the extrapolation. Through downward continuation, the locations of the shot and receivers are moved to sea bottom. (a) A shot gather prior to performing the downward continuation implies a short area of refractions. (b) However, a shot gather exhibits extended refraction signals after downward continuation.

2.2.2 Refraction tomography

For the explanation of refraction travel time tomography, we referred Yilmaz [2001[40]]. We want to describe the near-surface with the raypaths with minimal parameterization and consider the model shown in Figure 2.3. The travel time t'_{ij} for the refracted raypath from the shot location S_j to the receiver location R_i is given by

$$t'_{ij} = t_{S_jB} + t_{BC} + t_{CR_i}. \tag{2.32}$$

The first and the third terms are associated with the raypaths within the weathering layer and the second term is associated with the raypath within the bedrock along the refractor. In Figure 2.3, θ_c is the critical angle of refraction which is expressed in terms of the weathering and bedrock velocities by the relation $\theta_c = \sin^{-1}(v_w/v_b)$. The eqtuaion 2.32 can be rewritten in the following manner [De Amorim et al., 1987[10]]:

$$t'_{ij} = s_{wj}Z_j + s_{wi}Z_i + s_bX_{ij}, \tag{2.33}$$

where

$$Z_i = \frac{z_i}{\cos\theta_i}, \quad Z_j = \frac{z_j}{\cos\theta_j} \tag{2.34}$$

$$X_{ij} = x_{ij} - z_j\tan\theta_j - z_i\tan\theta_i \tag{2.35}$$

$$s_w = \frac{1}{v_w}, \quad s_b = \frac{1}{v_b}. \tag{2.36}$$

Consider an initial estimate of the parameter vector $\mathbf{p}$: $(\cdots, s_{wj}, \cdots, s_{wi}, \cdots, s_b)$. We want to minimize the difference between the observed and the modeled ti-

mes by iteratively perturbing the initial estimate of the parameter vector. A change Δp in the parameter vector will change the modeled times as follows:

$$\left[t'_{ij}\right]_{modeled} = \left[t'_{ij}\right]_{initial} + \left[\frac{\partial t'_{ij}}{\partial p}\right]_{modeled} \Delta p. \tag{2.37}$$

The error in modeling the traveltimes is given by

$$e_{ij} = \left[t_{ij}\right]_{observed} - \left[t'_{ij}\right]_{initial} - \left[\frac{\partial t'_{ij}}{\partial p}\right]_{modeled} \Delta p. \tag{2.38}$$

Now define the difference Δt_{ij} between the observed travel times t_{ij} and the initial estimate of the modeled tavel times t'_{ij}, and rewrite equation 2.38 to get

$$e_{ij} = \Delta t_{ij} - \frac{\partial t'_{ij}}{\partial p} \Delta p. \tag{2.39}$$

where

$$\Delta t'_{ij} = \frac{\partial t'_{ij}}{\partial p} \Delta p. \tag{2.40}$$

The derivatives $\partial t'_{ij}/\partial p$ in eqaution 2.39 can be computed by differentiating the model equation 2.33 with respect to each of the parameters:

$$\frac{\partial t'_{ij}}{\partial s_{wj}} \equiv Z_j, \quad \frac{\partial t'_{ij}}{\partial s_{wi}} \equiv Z_i, \quad \frac{\partial t'_{ij}}{\partial s_b} \equiv X_{ij}. \tag{2.41}$$

These then are substituted back into the right-hand side of eqaution 2.40 to get

$$\Delta t'_{ij} = Z_j \Delta s_{wj} + Z_i \Delta s_{wi} + X_{ij} \Delta s_b. \tag{2.42}$$

As shown upper, using difference of travel time between observed and simulated data, we can update velocity of each grid point. This scheme has merits

that it is free from amplitude of wavefield, because it only consider the travel times.

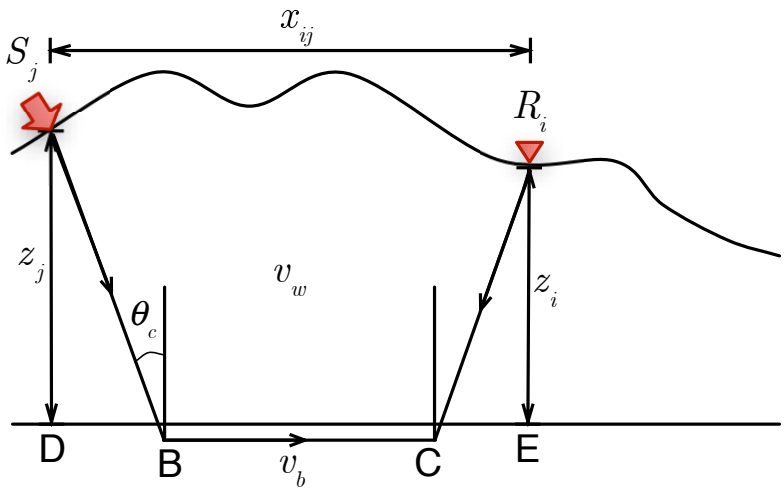

Figure 2.3: Geometry of refracted arrival used in deriving th least-squares solution for intercept times. Here, S_j and R_i are source and receiver stations, respectively; θ_c is the critical angle of refraction, z_j and z_i are depths to the bedrock at source and receiver locations, and v_w and v_b are weathering and bedrock velocities, respectively.

Chapter 3

Synthetic data examples

To verify the reliability of the scheme to create a macro-velocity model in an ultra deep-sea region, we performed the Laplace-Fourier inversion on two sets of synthetic data. The first is the Marmousi model, which implies several faults, folds and a trap structure. Though this model is a synthetic velocity model, it includes a variety types of geological structures. Thus, the Marmousi model is broadly used as a benchmark model. In this chapter, we added a water layer to the original velocity model to generate both shallow and deep-sea velocity models. We applied water-layer depths of 0.2 km and 3 km to the shallow and deep-sea models. By using a wave propagation-modeling scheme with both of the velocity models, we obtained time-domain seismic data. Based on this seismic data, we performed a Laplace-Fourier inversion. Then, to prove the reliability of the inverse velocity models, we presented reverse-time migration images obtained from using the inversion result as a background velocity model.

3.1 Marmousi with water layer

We generated a synthetic velocity model based on the original Marmousi model with a shallow water layer. The depth of the water layer in the shallow model was 0.2 km, and its velocity model is presented in Figure 3.1. The deep model consisted of water that was 3.0 km deep and is shown in Figure 3.2. The velocities ranged from 1.5 km/s to 5.5 km/s. We used a wave propagation-modeling scheme in this model to obtain the seismic data. For the wave propagation modeling in the time domain, we used a finite difference scheme with a fourth-order staggered grid [Graves et al., 1996[13]] and perfectly matched layer (PML) boundary conditions. The PML boundary exhibits high accuracy and a small noise reflector in half-space acoustic media. However, this form requires a first-derivative form in the spatial domain. Thus, a staggered grid must be applied that can calculate the pressure by separately computing the velocity and stress terms. A brief explanation of wave propagation with a staggered grid and a PML boundary is presented in Appendix A. To obtain the seismic data shown in Figures 3.3 and 3.4, we use a 5-m grid. The distances of the shot and receiver intervals were 100 m and 5 m, respectively. The number of the shot was 151. We assumed the length of streamer to be 6 km. The maximum frequency used in the model was 30 Hz, and we used a Ricker wavelet as a source function. The total exposure time was 4 s and 8 s in case of shallow- and deep-sea model, respectively. The time interval was 4 ms. For the stability of the wavefields, we used 0.5 ms in the modeling procedure and resampled the data at 4 ms.

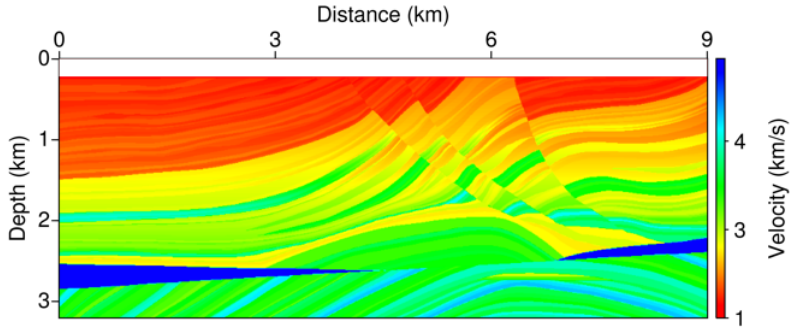

Figure 3.1: Marmousi velocity model with a shallow 0.2-km water layer.

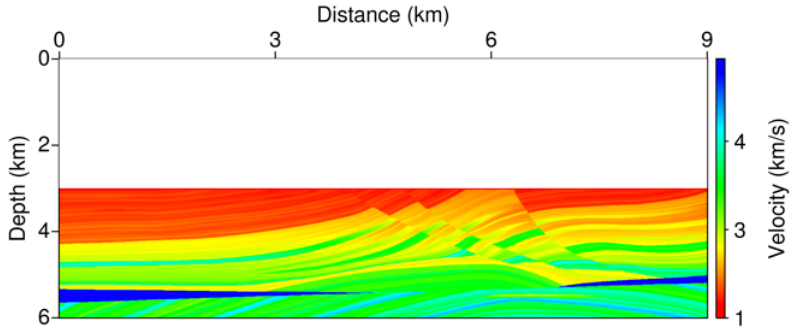

Figure 3.2: Marmousi velocity model with a 3.0-km-deep water layer.

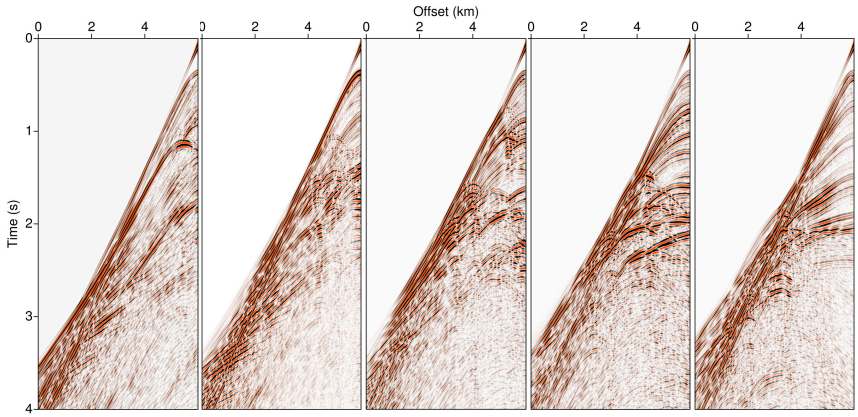

Figure 3.3: Seismic data obtained from the velocity model presented in Figure 3.1. The locations of shot gather from left-to-right are 5 km, 6 km, 7 km, 8 km and 9 km.

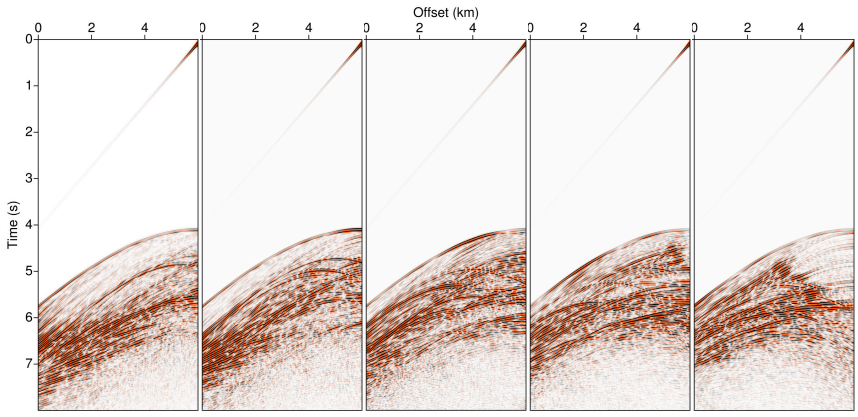

Figure 3.4: Seismic data obtained from the velocity model presented in Figure 3.2. The locations of the shot gather from left-to-right are 5 km, 6 km, 7 km, 8 km and 9 km. Compared to the shot gather presented in Figure 3.3, the time of first arrival is more than 4 seconds later because of the deep-sea layer.

3.2 Parameters for inversion

Based on the data presented in Figures 3.3 and 3.4, we performed an inversion in the Laplace-Fourier domain. We applied a finite element scheme to calculate the gradient and the virtual source using a back-propagation algorithm. For the inversion procedure, we set the maximum frequency as 15 Hz. The size of the element was 25 m $\times$ 25 m. The maximum and minimum velocities were set at 5.5 km/s and 1.5 km/s, respectively. The stabilizing factor was 10^{-6}. We used vertical linearly increasing velocity model as a starting model, and the velocity ranged from 1.5 km/s to 4.0 km/s. The ranges of the Laplace damping coefficient and the frequency component are shown in Table 3.1. For an efficient algorithm, we controlled the frequency group calculated as presented in Figure 3.5.

Table 3.1: Frequency loop used in Laplace-Fourier inversion of the Marmousi model.

	Laplace damping coefficients		**Frequency components**	
	Range	Interval	Range	Interval
1st part	$1 \sim 13$	2	$0.26 \sim 6.00$	0.25
2nd part		0.75	$0.25 \sim 5.25$	0.25
3rd part		0.50	$0.25 \sim 5.25$	0.25
4th part		0.15	$0.25 \sim 5.25$	0.25
5th part		0.10	$1.00 \sim 15.0$	0.25

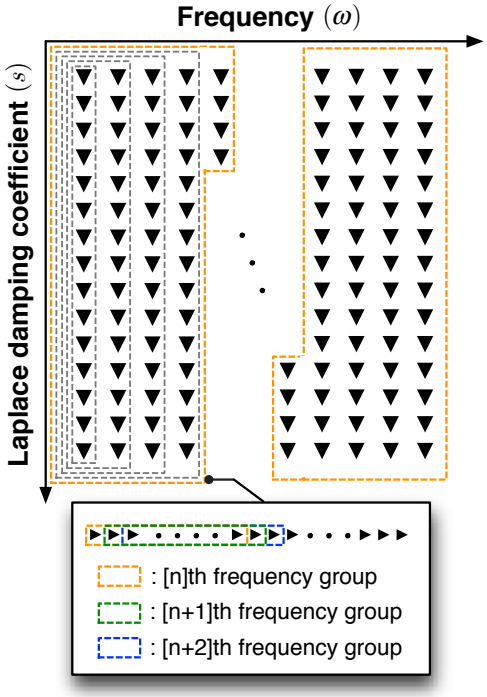

Figure 3.5: Conceptual diagram of the frequency loop grouped into 64 components combined with the damping coefficient and frequency.

3.3 Laplace-Fourier-domain inversion results

The Laplace-domain inversion is generally considered appropriate to recover the velocity structure in the area that relates to half the streamer length, a consideration based not on algebraic proof but from experimentation. The reason is as follows. If we use a damped wavefield, the value of the wavefield from the deeper region will be small, approximately zero. Thus, accurate computations of the residual value in deeper regions are problematic, and the gradient value can be inaccurate. An inexact gradient results in a distorted subsurface structure. Therefore, when we deal with the data from the ultra deep-sea region, we must consider the deep-water effect. We will demonstrate that the water layer may distort the subsurface structure from that determined using the Laplace-Fourier domain inversion. To adequately determine the effect of the water layer, we set the streamer length a relatively short value compared with the water depth. The maximum depth of the original model was 3 km, and we fixed the streamer length at 6 km in the Marmousi model, so that the ray path can cover the entire velocity model. If we add 3 km of water depth to original model, total depth of the velocity model will be 6 km. According to the general recoverable area in the Laplace-Fourier domain, approximately 3 km of structure will be constructed. We will provide several numerical examples as confirmation of this idea. To recover the velocity model, we chose the vertical linearly increasing velocity model as a starting model for the inversion. The velocity area of the initial model ranged from 1.5 km/s to 4.5 km/s. The procedures for the inversion in each model are presented in Figures 3.6, and 3.7.

Figure 3.6 shows recovering process of the model in shallow water. When we perform an inversion in the Laplace domain, the damping coefficient typically ranges from 1 to 15. In this test, we applied a range of damping coefficients from 1 to 13. With a damped wavefield, we can reduce the possibility of the convergence to local minima that can act as a major obstacle in conventional frequency-domain inversion. Based on the relatively large damping coefficients, we can obtain the macro-velocity model with a long wavelength as shown in Figures 3.6(b) and 3.7(b). After constructing the macro-velocity model, we performed an inversion with a low damping coefficient and a high frequency component that is similar to frequency-domain inversion. We obtained the final velocity model shown in Figures 3.6(c) and 3.7(c) after the 50th iteration. Because the length of the streamer was 6 km, we expected that a 3-km depth of the subsurface structure could be reliable. As shown in Figure 3.6(c), the final model is similar to the original model. However, the macro-velocity model presented in Figure 3.7(b) is severely distorted compared to original velocity model shown in Figure 3.2. The area around 3 km is recovered slightly, but the entire velocity structure is far from the original velocity model. The deeper region of model is severely distorted because of the inaccurate gradient that originates from the extremely small value of the damped wavefield.

To compare the magnitude of the velocities, we selected several target lines and plotted their velocity according to the depth. One of the principal objectives in the inversion test of the Marmousi model is the recovery of the trap structure and high velocity area located below the faults. Thus, we plotted four lines around the traps in the graph presented in Figure 3.8(a). The blue lines

indicate the original velocity values according to the depth. The red and green lines indicate the velocities from shallow- and deep-water data, respectively. As shown in the graph, the velocity recovered from the shallow water data has a similar tendency to that of the original model. However, the tendency of the green line from the deep-water data is far from that of the original model when the depth is greater than 1.0 km.

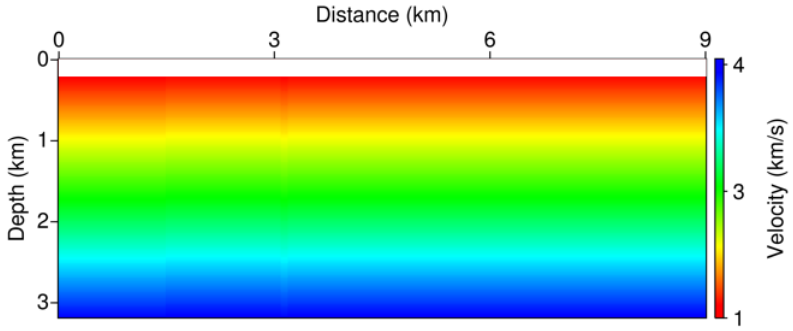

(a)

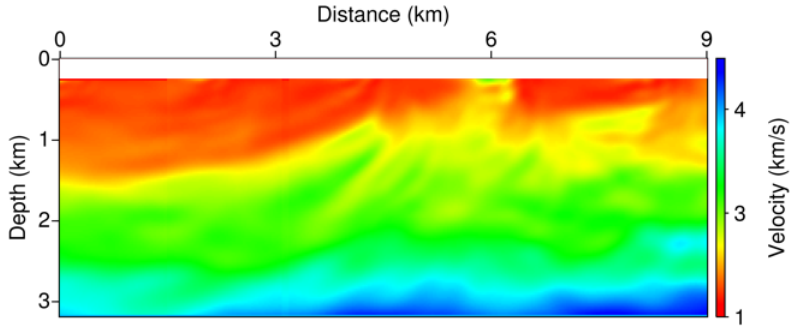

(b)

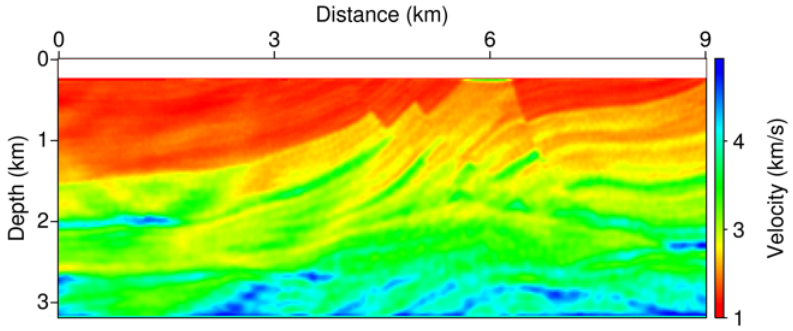

(c)

Figure 3.6: The procedure for the recovering velocity model using the Laplace-Fourier domain inversion. (a) The initial velocity model ranging from a velocity of 1.5 km/s to 4.5 km/s. (b) The inversed velocity model after the 37th loop. (c) The final inversed velocity model obtained through 50 iterations of the frequency-domain inversion.

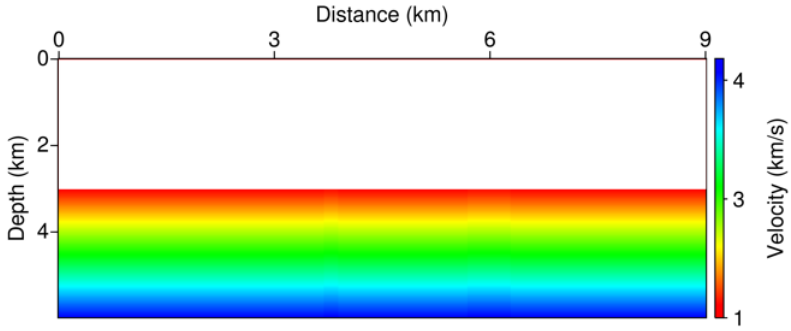

(a)

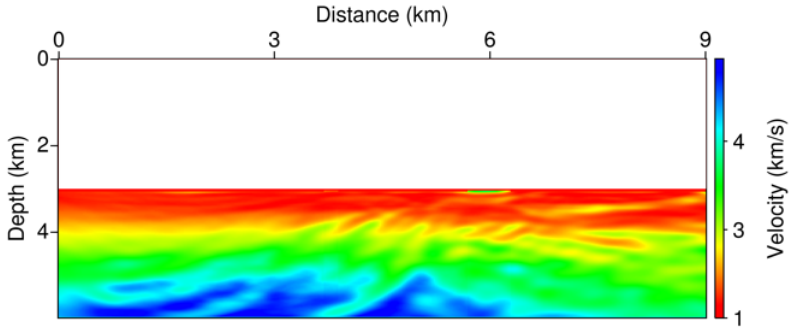

(b)

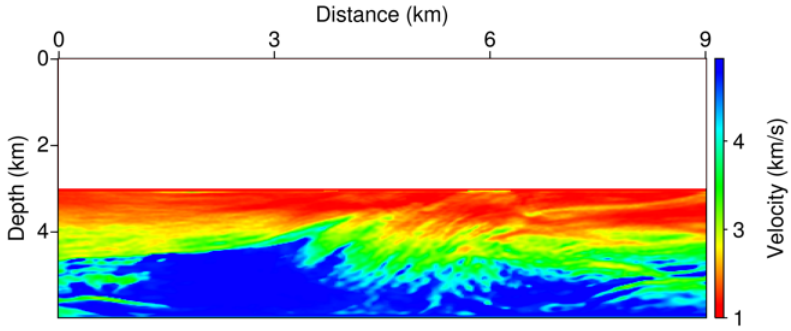

(c)

Figure 3.7: The procedure for recovering the velocity model using the Laplace-Fourier domain inversion. (a) The initial velocity model with velocities ranging from 1.5 km/s to 4.5 km/s. (b) The inversed velocity model after the 37th loop. (c) The final inversed velocity model obtained through 300 iterations of the frequency-domain inversion. When these results are compared with those in Figure 3.6(c).

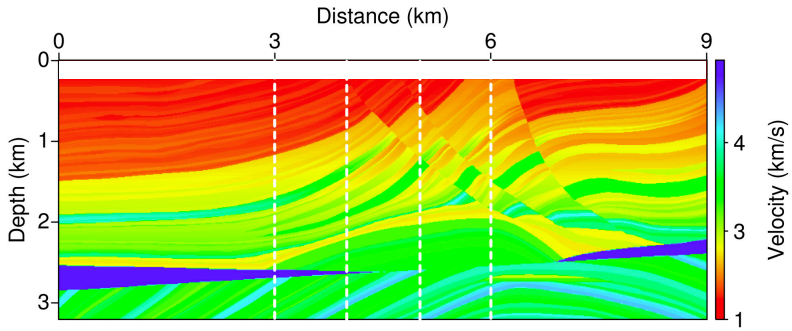

(a)

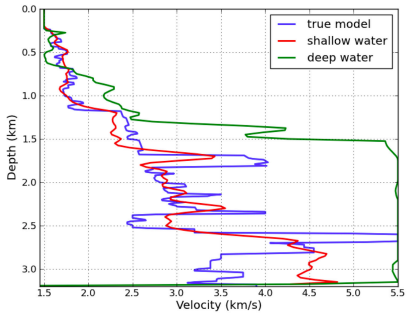

(b)

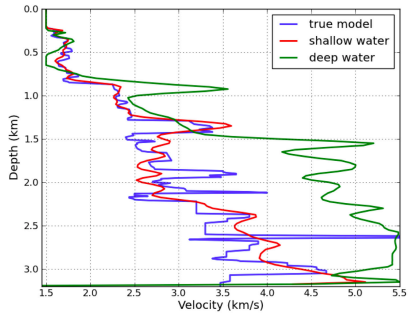

(c)

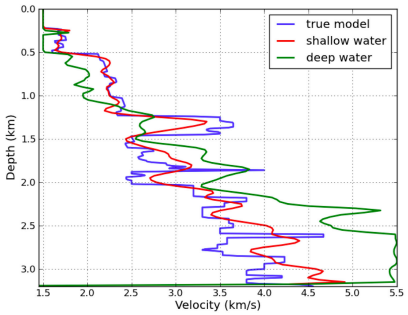

(d)

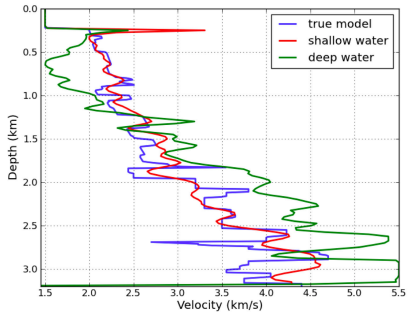

(e)

Figure 3.8: Comparison of the inversion results. (a) The original velocity model that we selected four lines around the traps from the left side at (b) 3 km, (c) 4 km, (d) 5 km and (e) 6 km. As shown in the graph, the velocity value from the shallow water inversion data has a similar tendency to that of the original inversion. However, the tendency of green line (the deep-sea data) differs dramatically from original model at depths greater than 1.0 km.

3.4 Recovering deep-sea Marmousi model

As we can identify through the test, when we deal with deep-sea seismic data with short-offset, it is difficult to calculate exact velocity structure using conventional scheme such as Laplace-Fourier or frequency-domain inversion. To build velocity model, we used refraction traveltime tomography which are not so sensitive to amplitude. Because this scheme uses only travel time information of first break. We approximated Laplace inversion to refraction tomography by fixing frequency and damping coefficient to 0.1 and 3, respectively. After damping of wavefields, most of signals are getting weak and first break are relatively emphasized, so this method can be regarded as refraction tomography scheme [Choi et al., 2004[6]]. After obtaining macro velocity model using tomography, we used this result as a starting model for the Laplace-Fourier-domain inversion.

3.4.1 Downward continuation for synthetic data

For the stable downward continuation, we removed direct-wave from original seismic data. For the first step, moving term of space and time is multiplied to original data to perform downward continuation in shot gather. Then, we did the same procedure in receiver gather. During this process, to use shots having the maximum number of fold, we used the whole data except the both side of shots located in the area corresponding the length of streamer. In this test, to fit the same target area of inversion and tomography, we extended 3 km of the initial part in tomography. After completing downward continuation, we eliminated the latter part of data having no signals. For the last process, we reconstructed direct-wave using source estimation based on the original data.

We presented the result of downward continuation in Figure 3.9.

3.4.2 Refraction tomography and inversion

Using downward continued data presented in Figure 3.9, we obtained refraction tomography result shown in Figure 3.10(a). To use this result as a starting model for Laplace-Fourier inversion, we extended the water layer as shown in Figure 3.10(b) to fit to the original data. The final inversion results after 100th iteration is presented in Figure 3.10(c). To compare the magnitude of velocity models more exactly, we presented velocity profiles in Figure 3.11 with the same selecting point as shown before. In the graph, the green- and red-line are from Laplce-Fourier inversion and refraction tomography with frequency inversion. Red-line is more closer to the original model than green one. Overall, large portion of geological structure is recovered better than the image from Laplace-Fourier inversion only. Though, deepest area is still not accurate, we obtained significantly enhanced quality of velocity image compared to conventional Laplace-Fourier-domain inversion. Based on these results we can expect that it is possible to apply to field data that will be shown in next chapter.

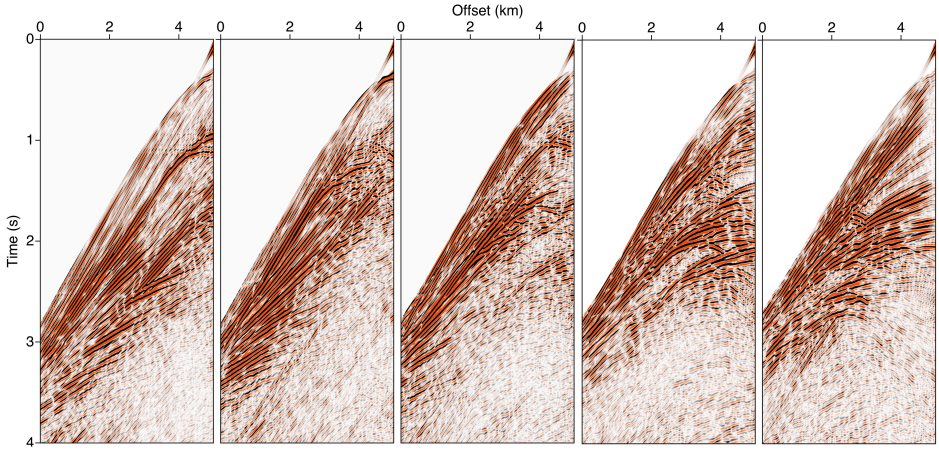

Figure 3.9: The locations of the shot gather from left-to-right are 5 km, 6 km, 7 km, 8 km and 9 km. Compared to the shot gather presented in Figure 3.4, the signal appears in early part.

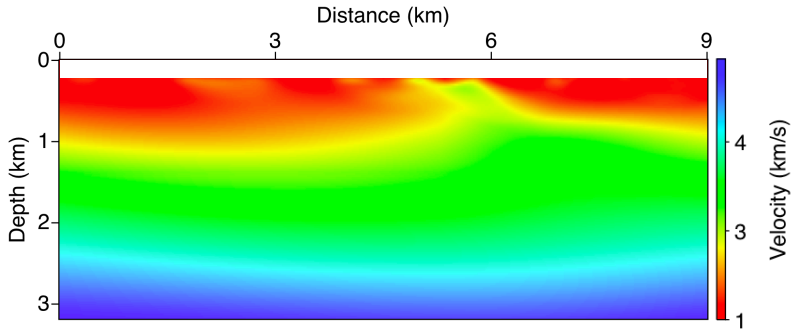

(a)

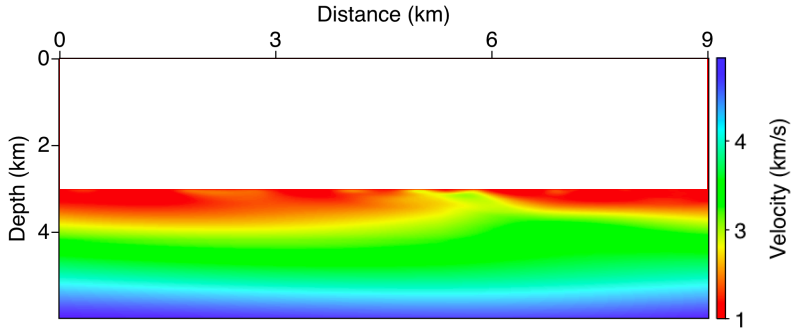

(b)

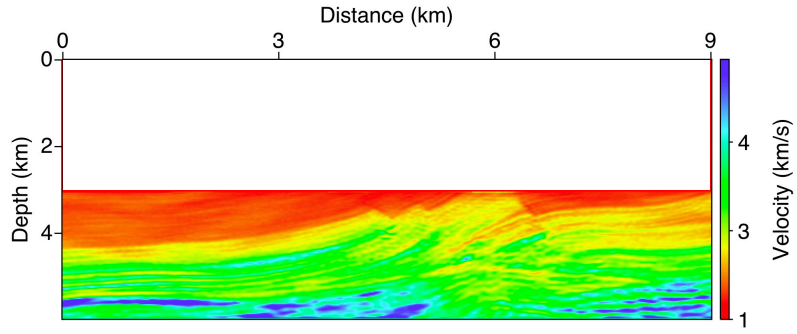

(c)

Figure 3.10: (a) Refraction tomography result using approximated scheme. (b) Extend water layer to fit the original deep-sea model. (c) Laplace-Fourier-domain inversion results using tomography result as a startig model.

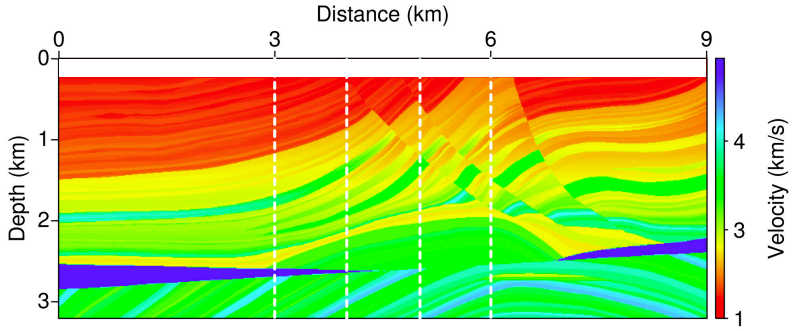

(a)

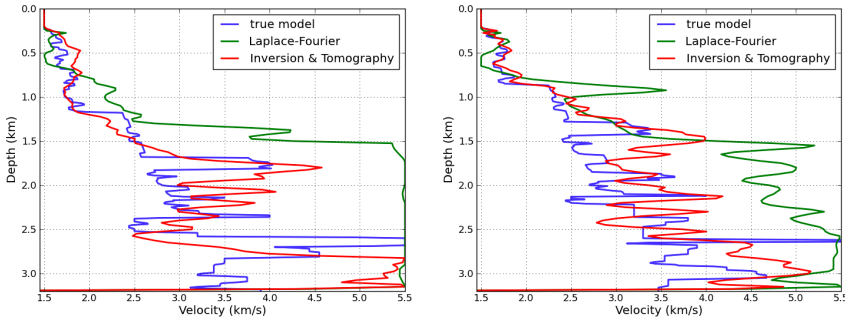

(b)

(c)

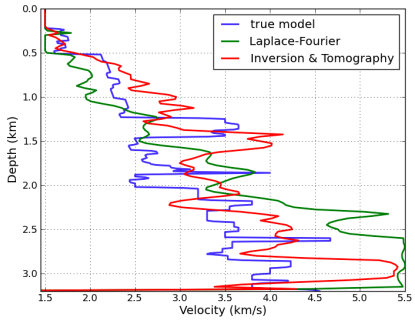

(d)

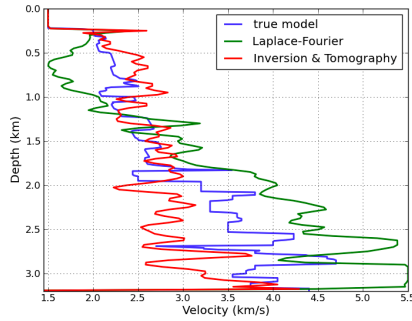

(e)

Figure 3.11: Comparison of the inversion results. (a) The original velocity model that we selected four lines around the traps from the left side at (b) 3 km, (c) 4 km, (d) 5 km and (e) 6 km. As shown in the graph, through the process of tomography and frequency-domain inversion, accuracy of result is significantly enhanced.

Chapter 4

Field data examples

4.1 Sumatra field data WG2 line

Sumatra (Indonesian: Sumatera) is the westernmost of the Sunda Islands in western Indonesia and is the largest island located entirely within Indonesia (two larger islands, Borneo and New Guinea, are shared between Indonesia and other countries). After the 2004 tsunami in this area, many studies have examined the origins of the Sumatra-Andaman earthquake and the strong movement of the subsurface structure. As a part of this study, seismic exploration was conducted by the CGGVeritas company, and the area of data acquisition is presented in Figure 4.1(a). Bathymetry data compiled by Henstock et al. [2006[17]] and Graindorge et al. [2008[12]] is superimposed onto the General Bathymetric Chart of the Oceans (GEBCO) grid in the image's background. The black line represents the WesternGeco seismic reflection profile WG2, the red dots indicate the OBS locations for the seismic refraction survey, and the brown dots indicate the Ocean Bottom Seismometer (OBS) locations for the aftershocks study [Sibuet et al., 2007[37]]. The red dotted contours represent the 10-m slip contour from Chlieh et al. [2007[5]], and the black dotted contours represent the 30-m slip contour from Rhie et al. [2007[31]] associated with the 2004 earthquake. The black dots are the aftershock locations, and the beach balls are the following Centroid-Moment-Tensor (CMT) solutions

corresponding to the earthquake locations from Engdahl et al. [2007[11]]: blue, thrust; green, strike-slip; and red, the normal faulting mechanism. The location of the 2004 great earthquake epicenter is marked by the large black beach ball. The WAF refers to the West Andaman Fault. The seismic image obtained through time-migration is shown in Figure 4.1(b).

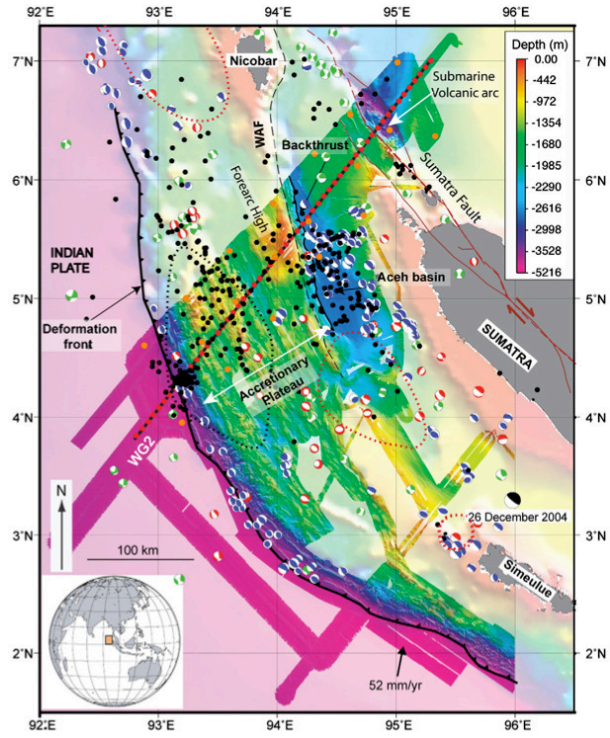

(a)

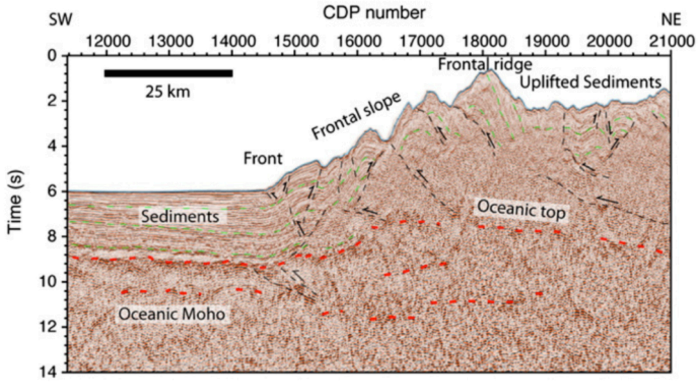

(b)

Figure 4.1: (a) The map of the study area (Sumatra, Indonesia). (b) The seismic image obtained through time-migration. Green lines: sediments; Red lines: Crustal and mantle reflectors; Black lines: faults and dipping reflectors.

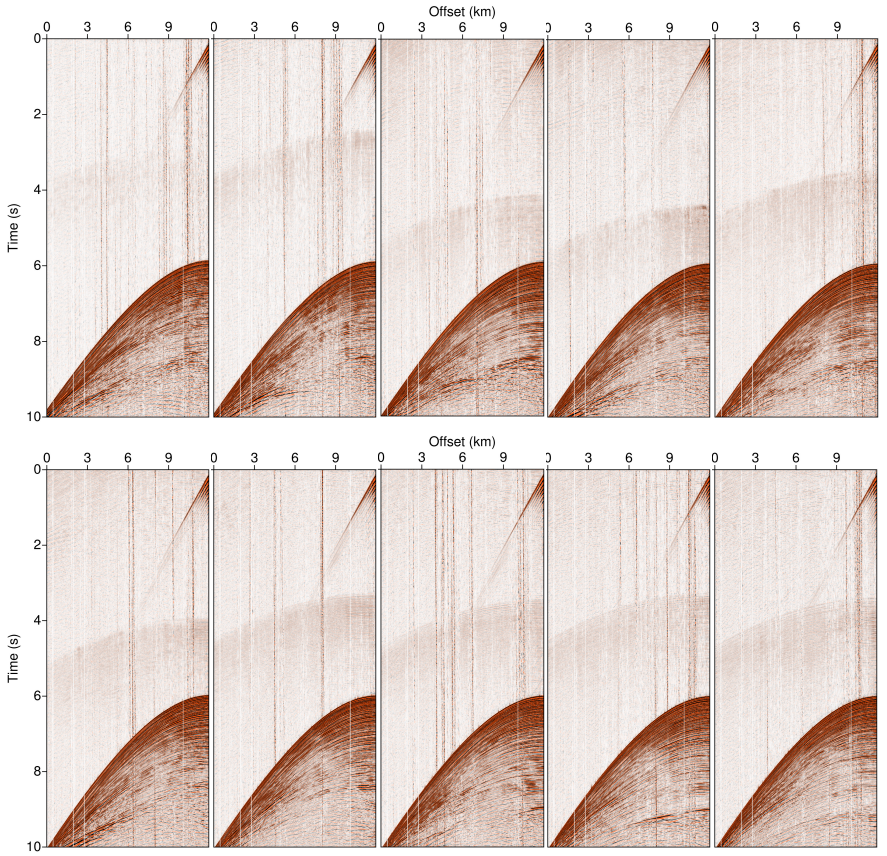

Figure 4.2: Shot profiles from the Sumatra data WG2 line. If we set the edge of left side as a standard point, the locations of the shot gathers are 12.25 km, 15.65 km, 19.05 km, 22.45 km, 25.85 km, 29.25 km, 32.65 km, 36.05 km, 39.45 km, 42.85 km, from left to right.

4.2 Preprocessing

To verify the method for building the velocity model in ultra deep-sea regions, we selected an oceanic portion of the seismic data that has a water layer of approximately 4.5 km. There were 1200 shots in the data set, and the shot interval was 50 m. The depth of the shot points was 10 m. The number of channels was 958, and the interval was 12.5 m. The near offset and far offset were 237.5 m and 12000 m, respectively. The receiver depth was 10 m from sea level. The total recording time was 20 s, and the sampling rate was 2 ms. Water velocity was fixed at 1498 m/s. Figure 4.2 shows several shot gathers from the Sumatra data WG2 line.

4.2.1 Direct-wave reconsturcion

The Laplace inversion requires damped wavefields because it is sensitive to the signals recorded near the first break. Thus, to obtain a reliable inversion result, muting is important. The Sumatra field data have a considerably thick seawater layer of 4.5 km with strong noises between the direct waves and their reflections. In addition, in the far-offset region, the amplitude of the direct wave is too weak for muting. Thus, we considered only the reflections and refractions, not the direct wave [Koo et al., 2011[20]]. We then reconstructed the direct wave after muting. The procedure for direct-wave reconstruction is presented in Figure 4.3.

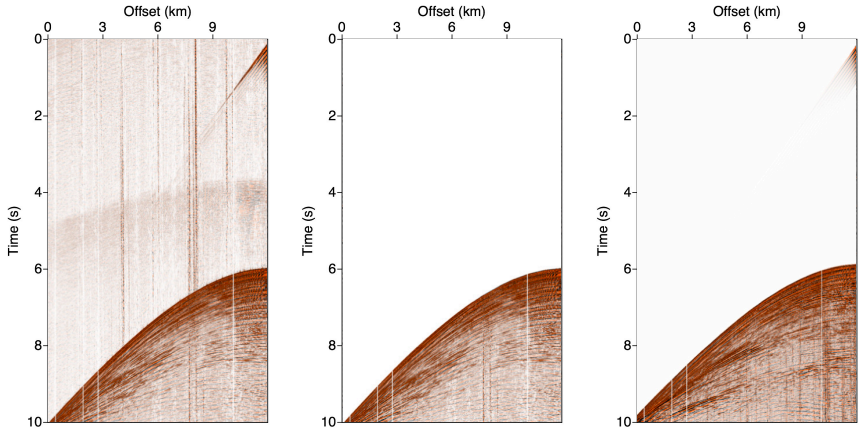

Figure 4.3: Procedure for the direct-wave reconstruction. After muting, prior to the arrival of the first reflection signals, we computed the direct-wave using a source estimation scheme. (a) A sample of the original shot gather, (b) the muted shot gather, and (c) the direct-wave reconstructed shot gather.

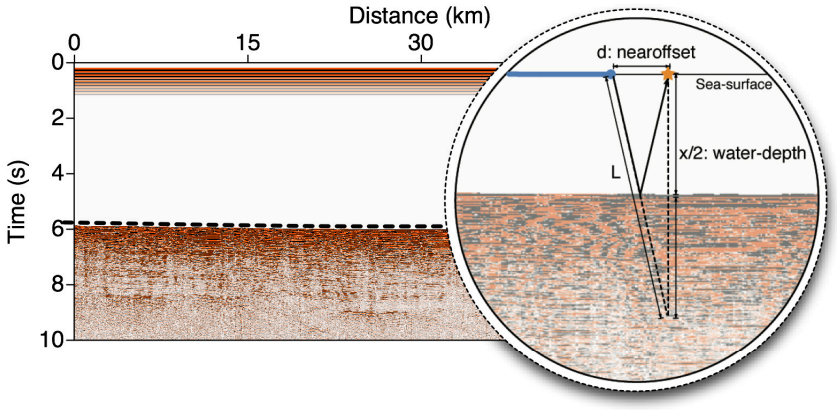

Figure 4.4: The seawater depth information was calculated from the near-offset gather image. The dotted line represents the selected time points. From these points, the seawater depth can be computed by setting the water velocity at 1498 m/s.

4.2.2 Defining sea-water depth

During inversion, the water layer is not considered in the velocity updating. Incorrect seawater depth data can cause artifacts near the surfaces, distorting the other aspects of the results. We calculated the seawater depth through the near-offset gather presented in Figure 4.4. After selecting the first arrival in the near-offset gather, which is shown as a black dotted line in Figure 4.4, the velocity of water layer was fixed at 1498 m/s. Given these data, we can compute the water-depth as $x/2 = \sqrt{l^2 - d^2}/2$. However, in deep-sea regions, the water velocity depends strongly on the location. Thus, during the calculation of seawater depth, a fixed water velocity may yield incomplete depth information.

4.2.3 Defining source wavelet

To calculate exact residual for the inversion, we must accurately define the source wavelet. In this study, we utilized a source estimation scheme using a direct wave. In the field data, however, the shape of the source function differs according to the direction of the source. Figure 4.5(a) shows direct wave signal, which is the horizontal source function, and Figure 4.5(b) shows the vertical source function observed during acquisition. This figure demonstrates that the two source functions have different shapes. Thus, the conventional method, which uses a source estimation scheme with a direct wave, cannot yield reliable results in this case. Therefore, we used source estimation only for scaling the amplitude of the source wavelet and performed the inversion and migration using the vertical-direction wavelet presented in Figure 4.5(b).

4.2.4 Downward continuation for field data

To perfrom refraction tomography without deep-water effect, we applied downward continuation on field data. The entire procedure is same as shown in the chapter of synthetic data test. Downward continued data shown in Figure 4.6 is used to obtain macro velocity model for the starting model of Laplace-Fourier inversion. After getting long wavelength velocity model through refraction tomography with downward continued data, we perform Laplace-Fourier inversion with original field data. These results will be shown in next section.

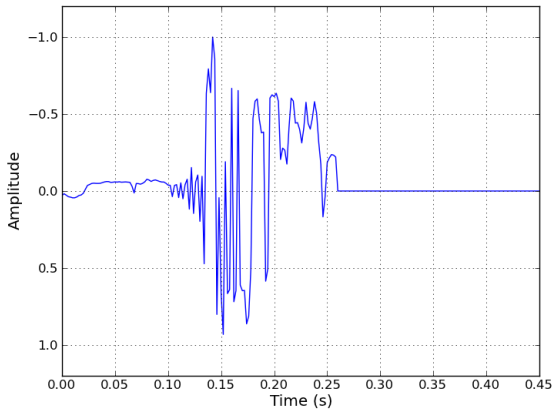

(a)

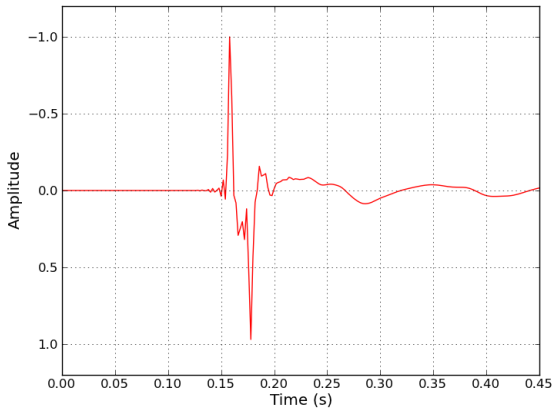

(b)

Figure 4.5: Shape of the source wavelet according to the direction: (a) horizontal, (b) vertical.

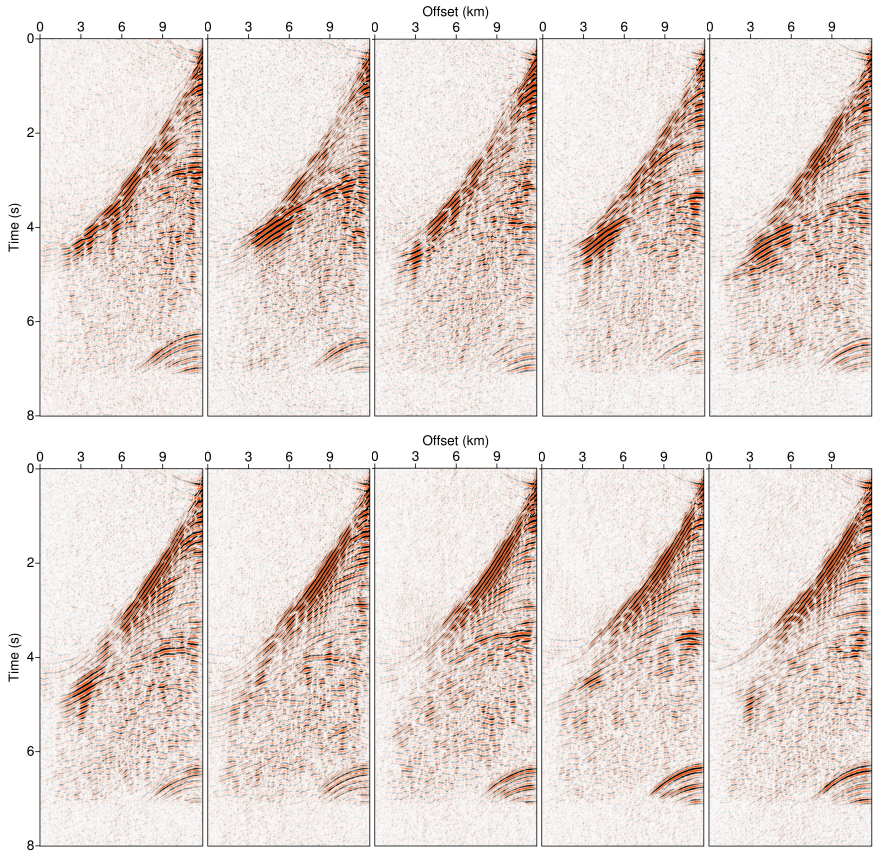

Figure 4.6: Shot profiles from the Sumatra data WG2 line following downward continuation. If we suppose the edge of left side as a standard point, the locations of the shot gather are 12.25 km, 15.65 km, 19.05 km, 22.45 km, 25.85 km, 29.25 km, 32.65 km, 36.05 km, 39.45 km and 42.85 km from left to right.

4.3 Construction of velocity model

4.3.1 Laplace-Fourier-domain inversion

We performed a Laplace-Fourier-domain inversion using the dataset presented in Figure 4.3(c). For the frequency-domain modeling, we used the finite element scheme and applied a 25-m grid interval for the interpolation. The frequency loop used was that presented in Table 3.1. We used a linearly increasing model whose velocity varied from 1.9 km/s at the sea floor to 6.0 km/s at a depth of 11 km as the initial model presented in Figure 4.7(a).

4.3.2 Frequency-domain inversion with tomography

We performed refraction tomography with 50 m of grid size using downward continued data. After obtaining a macro-velocity model through refraction tomography, we performed a frequency-domain inversion based on the tomography results. The inversion was implemented sequentially using 5 complex angular frequencies with the imaginary portion fixed at 1.0 and a real portion with values ranging from 4 to 12 Hz at intervals of 2 Hz.

4.3.3 Inversion results

Laplace-Fourier-domain inversion results updated from the initial model are presented in Figures 4.7 and 4.8, respectively. For a clear distinction of the sea floor, we eliminated the water layer with a velocity of 1.5 km/s from the results. The results from the linearly increasing starting model shown in Figure 4.7 indicated that a thin low-velocity layer is located at a depth of approximately 6 km. In addition, an abnormal area of high velocity exists at a

distance of approximately 35 km. This result is based on the starting model from tomography that has an inclined high-velocity basement below 8 km. Compared with the results presented in Figure 4.8, no abnormal structure of high or low velocity exists around the shallow region of the structure. However, we observed a thin layer with a lower-velocity layer compared to that of the fringe area at a depth of approximately 9 km. As we compare these two results, we find that the overall tendencies in their subsurface structures are similar. However, several regions exhibit different structures, and to compare these results more precisely, we present the velocity-depth graph in Figure 4.10. The points selected for the velocity comparison are shown in Figure 4.9. Both results have similar trends in their points at both ends; however, they have significantly different features at the other chosen points. To assess the reliability of the inversion results, we performed a Kirchhoff depth migration having strength to accommodate layered media than reverse-time migration. The results of the depth migration are provided in next section.

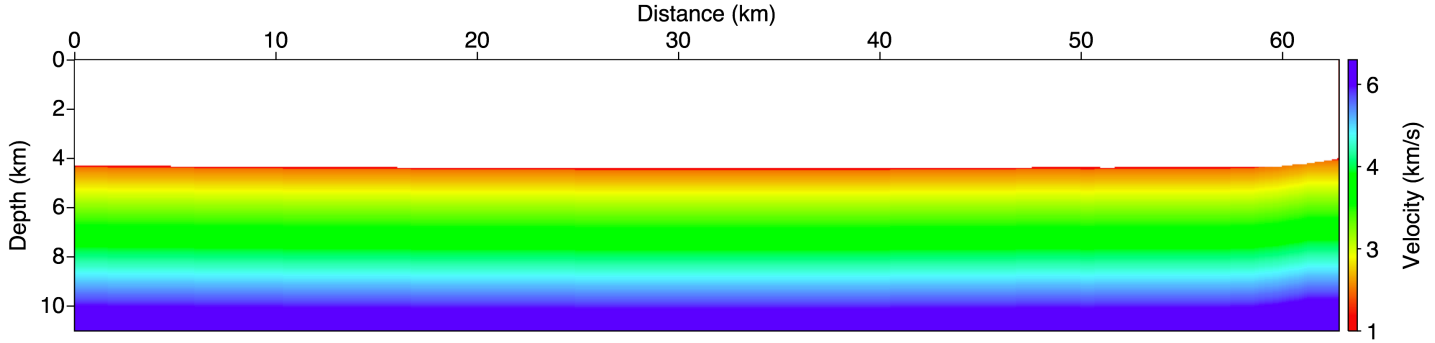

(a)

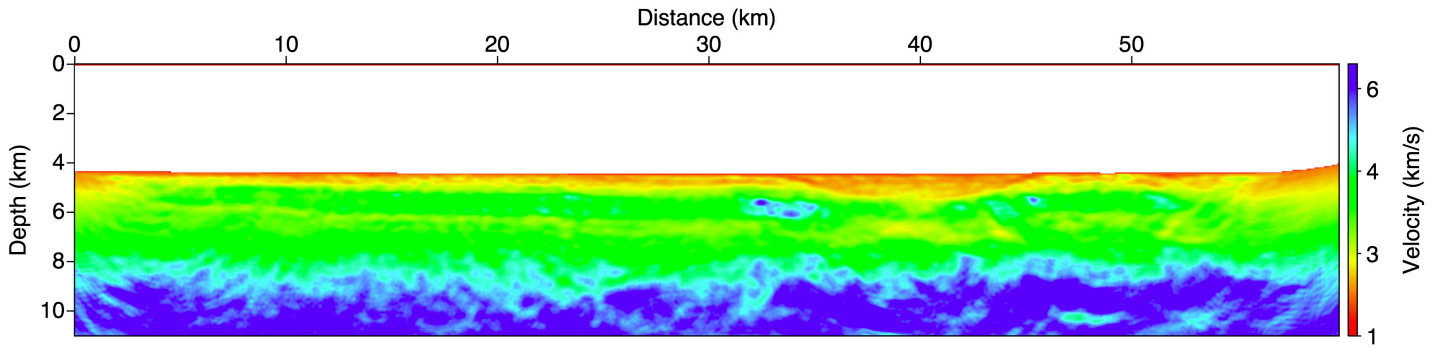

(b)

Figure 4.7: (a) Initial velocity model for the Laplace-Fourier inversion. (b) Laplace-Fourier inversion results after the 31th iteration.

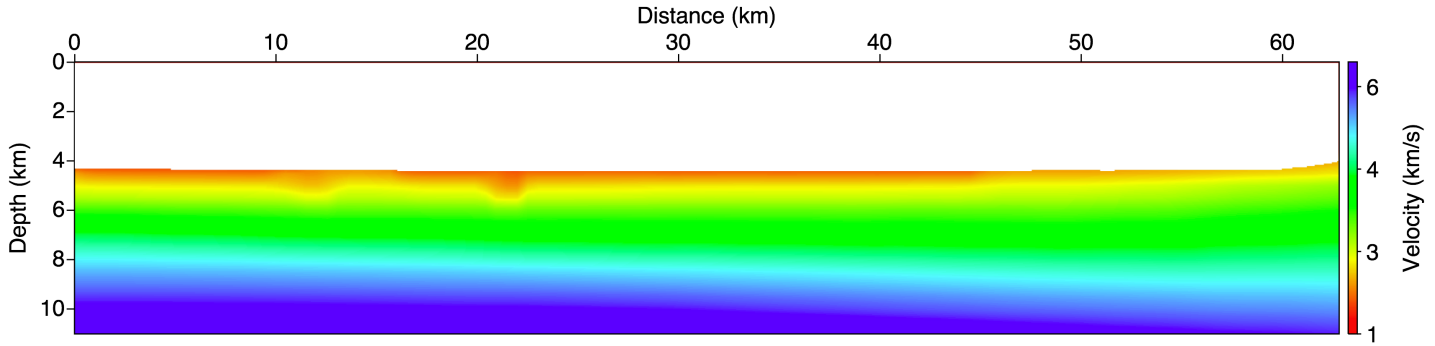

(a)

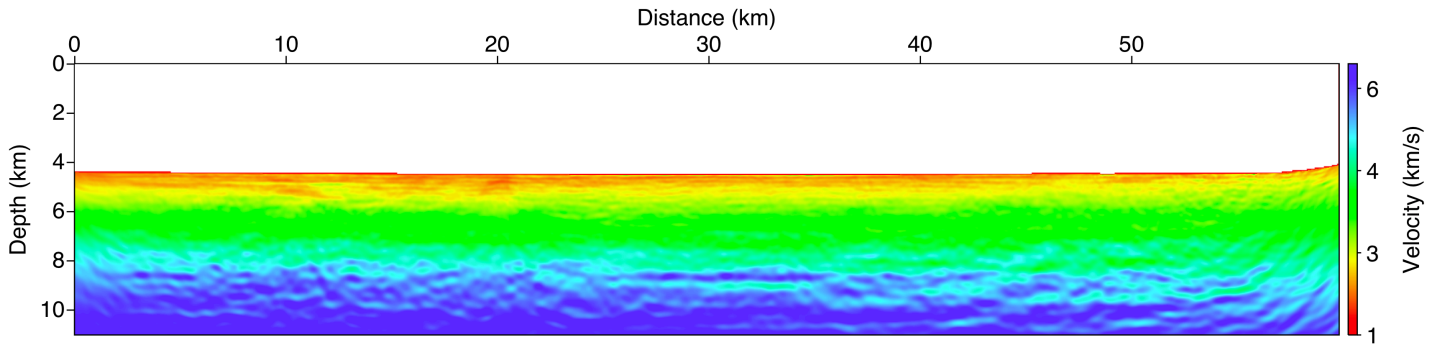

(b)

Figure 4.8: (a) Macro-velocity model obtained by refraction tomography using a downward-continued wavefield. (b) The Laplace-Fourier inversion results after the 36th iteration.

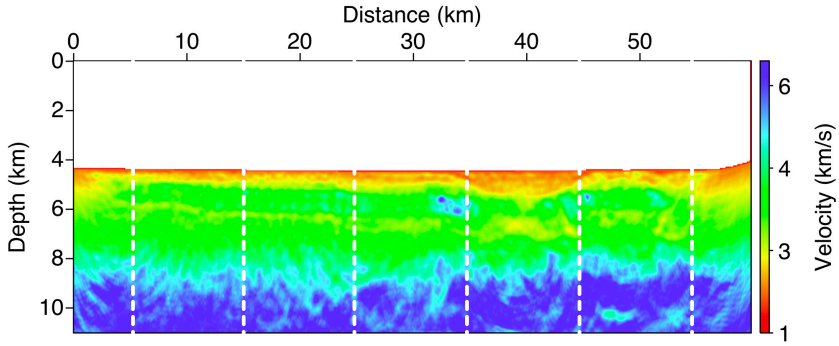

(a)

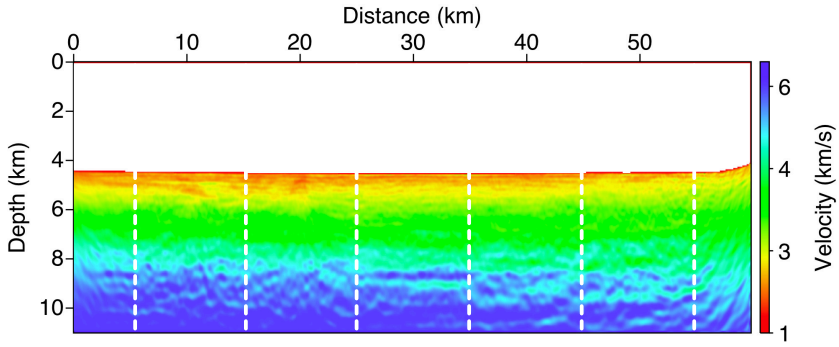

(b)

Figure 4.9: Selecting points to compare the inversion results. The magnitudes of the velocities corresponding to white dotted lines are presented in Figure 4.10.

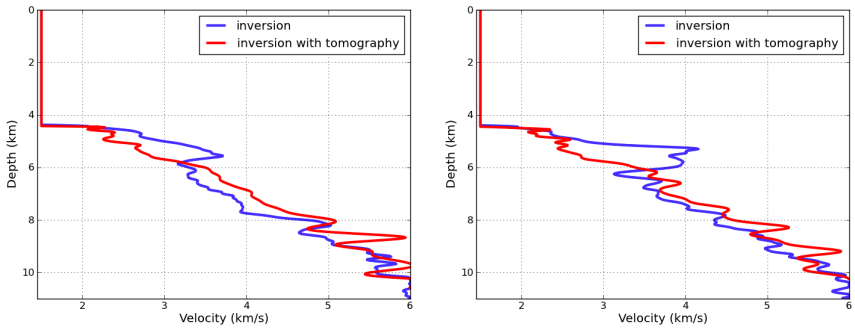

(a)

(b)

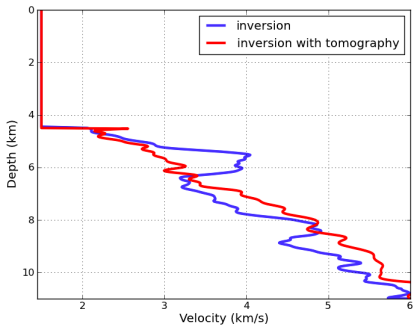

(c)

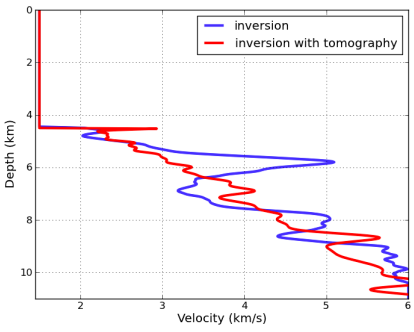

(d)

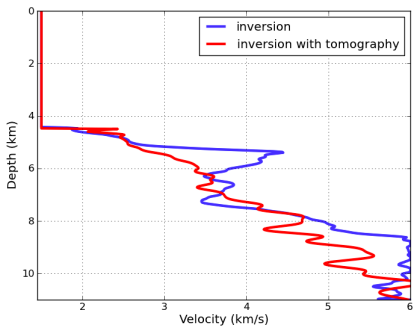

(e)

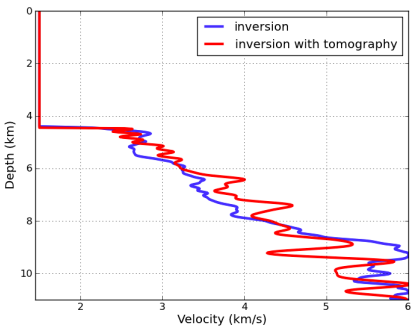

(f)

Figure 4.10: Comparison of the velocities corresponding to the white dotted lines presented in Figure 4.9. We selected six lines at even intervals: (a) 5 km, (b) 15 km, (c) 25 km, (d) 35 km, (e) 45 km and (f) 55 km from left to right. The blue and red lines indicate the Laplace-Fourier inversion results and the inversion results combined with tomography, respectively.

4.4 Migration

4.4.1 Parameters for migration

For the Kirchhoff depth migration, we used the original data with a 2-ms time-sampling interval. For the migration, we interpolated each inversion result to a 12.5-m grid interval. Several methods can be used to calculate travel time including SWEET [Min and Shin, 2006[24]], and the downward-continuation scheme; we applied the downward-continuation scheme [Claerbout, 2009[7]].

4.4.2 Kirchhoff depth migration results

We presented Kirchhoff depth migration results in Figure 4.11 and 4.12, respectively. Figure 4.11 is from Laplace-Fourier-domain inversed velocity model. As we can see in the image, the basement around 40 km of distance are folded severly. However, Figure 4.12 which is from combination of Laplace-Fourier-domain inversion and refraction tomography, shows clear and flat basement structure. Also, we can see clear fault structure in overall area. For exact analysis, we gathered common image points which are presented in Figure 4.13 and 4.14. The shape of common image gather (CIG) from Laplace-Fourier-domain inversion is curved to downward, which means magnitude of background velocity is lower than exact value. Comparing to the CIGs shown in Figure 4.13, Figure 4.14 shows more clear and flat shape of image points. It means the background velocity model is quit exact for depth migration.

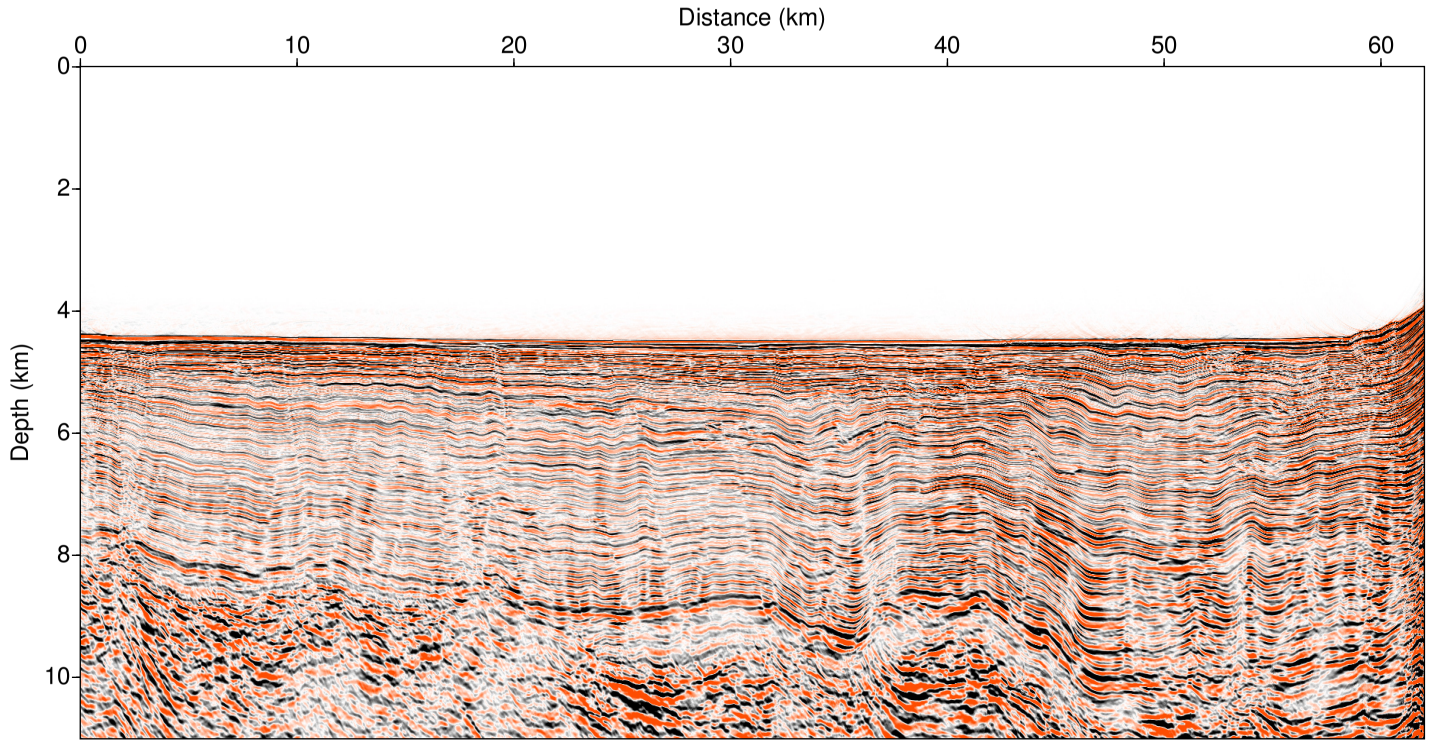

Figure 4.11: Kirchhoff depth migration results based on the velocity model obtained through a Laplace-Fourier inversion.

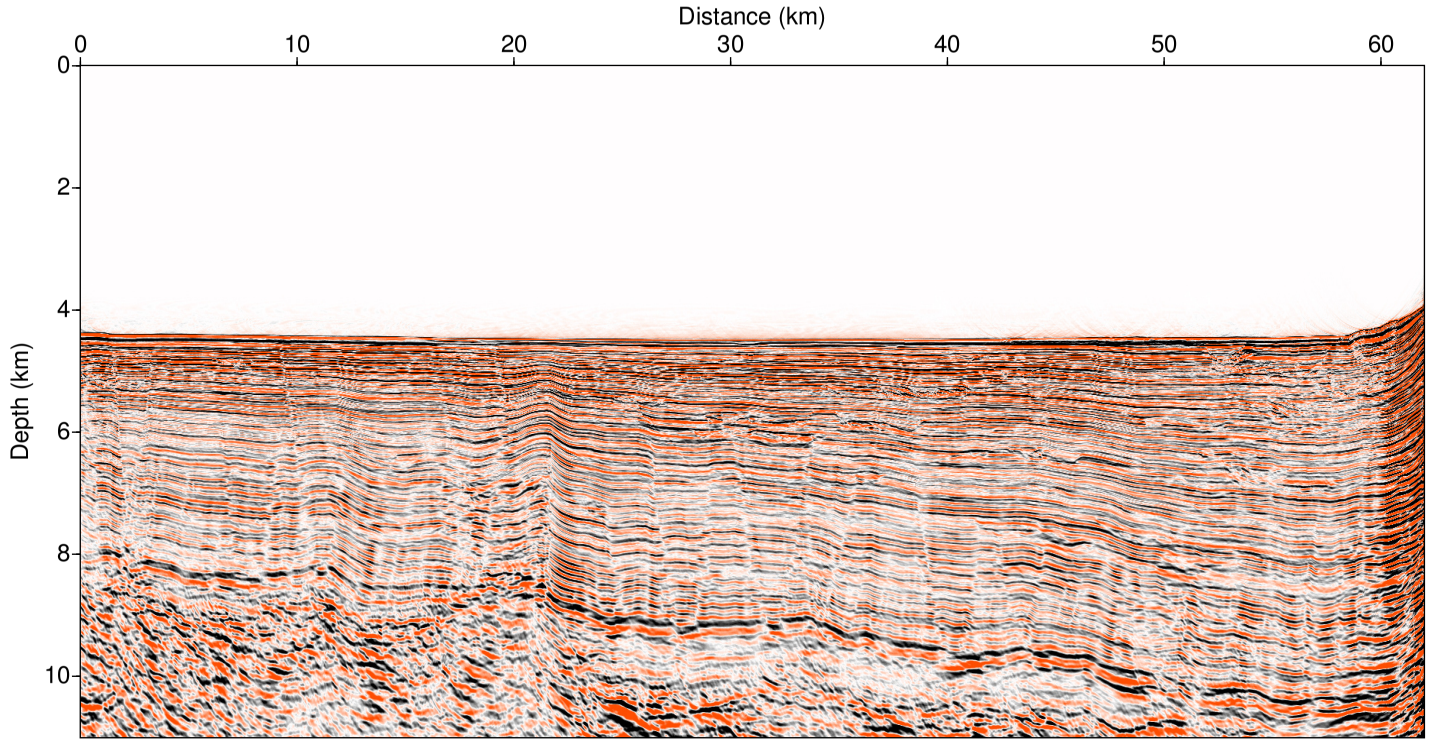

Figure 4.12: Kirchhoff depth migration results based on the velocity model obtained through a combination of tomography and the Laplace-Fourier inversion.

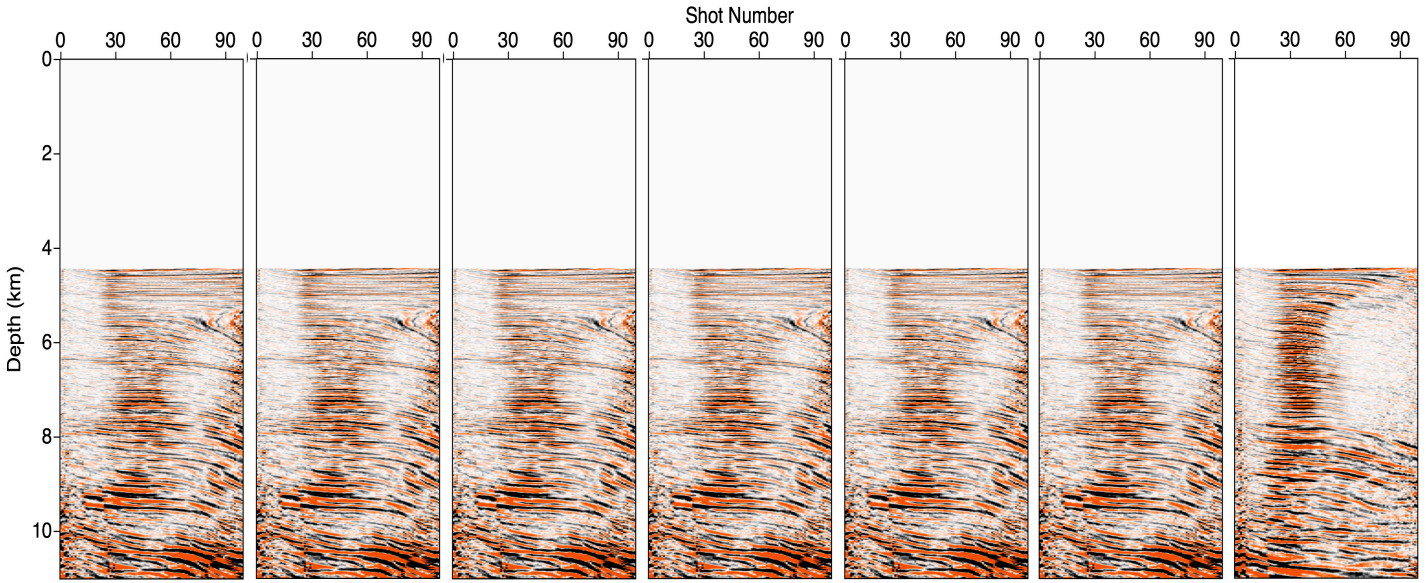

Figure 4.13: Common image gather from the Kirchhoff depth migration results presented in Figure 4.11. The positions of imaging points are 25 km, 31.25 km, 37.5 km, 43.75 km, 50 km, 56.25 km, and 62.5 km from left to right.

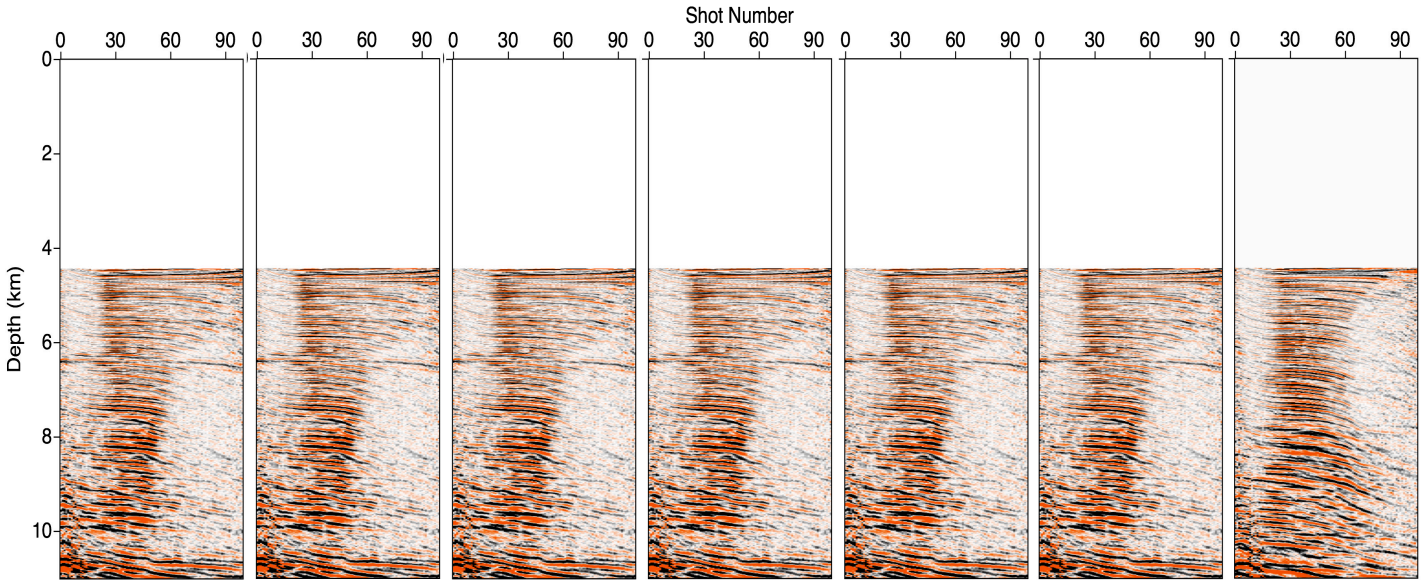

Figure 4.14: Common image gather from the Kirchhoff depth migration results presented in Figure 4.12. The imaging points are positioned at 25 km, 31.25 km, 37.5 km, 43.75 km, 50 km, 56.25 km, and 62.5 km from left to right.

Chapter 5

Conclusion

In this study, we attempted to build a reliable velocity model for deep-sea seismic data with a short-offset. For the first inversion method, we performed the well-known Laplace-Fourier inversion to calculate the subsurface velocity structure. Using the Laplace-Fourier inversion for deep-sea data, however, is difficult because of the damped wavefield in the Laplace domain that can yield inaccurate residuals and gradients. Therefore, with this method, we could not obtain an exact velocity structure of deep-water region. As an alternative, we applied a wavefield extrapolation with downward continuation to eliminate the water effect. We then performed refraction tomography using extrapolated seismic data. In addition, to increase the resolution of the tomography results, Laplace-Fourier-domain inversion was performed. We determined that the refraction tomography with downward-continued data and the frequency-domain inversion can recover the subsurface structure located at considerable depths through experiments using both synthetic and field data. For the synthetic data, velocity structure was successfully calculated and found to be the same as original velocity model. When we applied our scheme to the field data to verify the inversion results, we performed a Kirchhoff depth migration based on the velocity model obtained through inversion and tomography. We identified common image gathers of the migration using tomography that are quite flat compared with those from the Laplace-Fourier inversion. The

downward-continuation scheme used in this study increased the amplitude of the refractions but distorted the reflections after extrapolation. In addition, the two end regions of the data that correspond to the length of streamer were unusable because of inconsistency of the number of extrapolated traces. Thus, a more stable extrapolation scheme is required for the application of downward-continued data to a full waveform inversion.

Chapter 6

Appendix A.

A.1 Application of Perfectly Matched Layer in time domain

For almost all cases of the wave-propagation model, we assumed an infinite space except for the free-surface side, necessitating the use of proper boundary conditions. A variety of boundary conditions such as Higdon [Higdon, 1986[18]] and Clayton-Anquist [Clayton and Anquist, 1977[9]] have been used for this simulation. However, the perfectly matched layer (PML) is among the most powerful schemes for absorbing a boundary without generating other reflections around the boundary. As a first step in applying the PML for acoustic media in the time domain, we can write the 2D elastodynamics problem as a first-order hyperbolic system, the so-called velocity-stress system:

$$\begin{aligned} \rho \frac{\partial v}{\partial t} - \mathbf{div}\sigma = 0, \\ A \frac{\partial \sigma}{\partial t} - \varepsilon(v) = 0, \end{aligned} \tag{A-1}$$

in which v denotes the p-wave velocity, σ the stress tensor and ρ the density. If $u = (u_x, u_y)$ is the displacement, then $v = \frac{\partial u}{\partial t}$. We denote $\varepsilon(u)$ as the deformation tensor, i.e.,

$$\varepsilon_{ij}(u) = \frac{1}{2}\left(\frac{\partial u_i}{\partial x_j} + \frac{\partial u_j}{\partial x_i}\right). \tag{A-2}$$

The stress tensor is related to the deformation tensor by Hooke's law

$$\sigma = \sigma(u)(x,t) = C(x)\varepsilon(u)(x,t), \tag{A-3}$$

in which $C(x)$ is a positive tensor with the classical properties of symmetry, and the A term presented in equation A-1 can be written as $A = A(x) = C^{-1}(x)$. Based on the previously presented system, we can obtain the following system in the perfectly matched layer $(x > 0)$

$$\begin{aligned} & v = v^{\parallel} + v^{\perp}, \\ & \rho \frac{\partial v^{\parallel}}{\partial t} = D^{\parallel} \frac{\partial \sigma}{\partial y}, \\ & \rho \frac{\partial v^{\perp}}{\partial t} + d(x) v^{\perp} = D^{\perp} \frac{\partial \sigma}{\partial x}, \end{aligned} \tag{A-4}$$

and

$$\begin{aligned} & \sigma = \sigma^{\parallel} + \sigma^{\perp}, \\ & A \frac{\partial \sigma^{\parallel}}{\partial t} = E^{\parallel} \frac{\partial v}{\partial y}, \\ & A \frac{\partial \sigma^{\perp}}{\partial t} + d(x) A \sigma^{\perp} = E^{\perp} \frac{\partial v}{\partial x}, \end{aligned} \tag{A-5}$$

in which $d(x)$ denotes the damping factor. The symbol $\parallel$ indicates that we retain only the derivative parallel to the interface. For example, $\parallel$ denotes the y-derivative, while the index $\perp$ indicates that only the x-derivative is considered. In an isotropic acoustic medium, equation A-1 can be written as follows:

$$\begin{aligned} & \rho \frac{\partial v_x}{\partial t} = \frac{\partial \sigma_x}{\partial x} \quad ; \quad \frac{\partial \sigma_x}{\partial t} = \rho v^2 \left(\frac{\partial v_x}{\partial x} + \frac{\partial v_y}{\partial y} \right), \\ & \rho \frac{\partial v_y}{\partial t} = \frac{\partial \sigma_y}{\partial y} \quad ; \quad \frac{\partial \sigma_y}{\partial t} = \rho v^2 \left(\frac{\partial v_y}{\partial y} + \frac{\partial v_x}{\partial x} \right), \end{aligned} \tag{A-6}$$

and the PML system in the 2D acoustic media becomes

$$\begin{aligned}
\left(\frac{\partial}{\partial t}+d(x)\right)\sigma_x^{\perp} &= \rho v^2\frac{\partial v_x}{\partial x} \quad ; \quad \frac{\partial \sigma_x^{\parallel}}{\partial t} = \rho v^2\frac{\partial v_y}{\partial y},\\
\left(\frac{\partial}{\partial t}+d(x)\right)\sigma_y^{\perp} &= \rho v^2\frac{\partial v_x}{\partial y} \quad ; \quad \frac{\partial \sigma_y^{\parallel}}{\partial t} = \rho v^2\frac{\partial v_y}{\partial y},
\end{aligned} \tag{A-7}$$

To apply this boundary condition in the time domain, we use the staggered grid [Graves, 1996[13]] formulation presented in Figure A-1 such that, if v_x is computed at the points (i,j) on a grid, then v_y is computed at the points $(i+\frac{1}{2}, j+\frac{1}{2})$, σ_x and σ_y are computed at $(i+\frac{1}{2}, j)$. The discrete form of the time-domain PML with a staggered grid can be written as follows:

$$\begin{aligned}
&\frac{(v_x)_{i,j}^{n+1}-(v_x)_{i,j}^{n}}{\Delta t}+d_i^x\frac{(v_x)_{i,j}^{n+1}+(v_x)_{i,j}^{n}}{2} = \frac{(\sigma_x)_{i^{\rightarrow},j}^{n+\frac{1}{2}}-(\sigma_x)_{i^{\leftarrow},j}^{n+\frac{1}{2}}}{\rho\Delta x},\\
&\frac{(v_y)_{i^{\rightarrow},j^{\rightarrow}}^{n+1}-(v_y)_{i^{\rightarrow},j^{\rightarrow}}^{n}}{\Delta t}+d_{j^{\rightarrow}}^y\frac{(v_y)_{i^{\rightarrow},j^{\rightarrow}}^{n+1}+(v_y)_{i^{\rightarrow},j^{\rightarrow}}^{n}}{2} = \frac{(\sigma_x)_{i^{\rightarrow},j^{\rightrightarrows}}^{n+\frac{1}{2}}-(\sigma_y)_{i^{\rightarrow},j}^{n+\frac{1}{2}}}{\rho\Delta y},
\end{aligned} \tag{A-8}$$

$$\begin{aligned}
&\frac{(\sigma_x)_{i^{\rightarrow},j}^{n+\frac{1}{2}}-(\sigma_x)_{i^{\rightarrow},j}^{n-\frac{1}{2}}}{\Delta t}+d_{i^{\rightarrow}}^x\frac{(\sigma_x)_{i^{\rightarrow},j}^{n+\frac{1}{2}}+(\sigma_x)_{i^{\rightarrow},j}^{n-\frac{1}{2}}}{2} = \rho v^2\frac{(v_x)_{i^{\rightrightarrows},j}^{n}-(v_x)_{i,j}^{n}}{\Delta x},\\
&\frac{(\sigma_y)_{i^{\rightarrow},j}^{n+\frac{1}{2}}-(\sigma_y)_{i^{\rightarrow},j}^{n-\frac{1}{2}}}{\Delta t}+d_j^y\frac{(\sigma_y)_{i^{\rightarrow},j}^{n+\frac{1}{2}}+(\sigma_y)_{i^{\rightarrow},j}^{n-\frac{1}{2}}}{2} = \rho v^2\frac{(v_y)_{i^{\rightarrow},j^{\rightarrow}}^{n}-(v_y)_{i^{\rightarrow},j^{\leftarrow}}^{n}}{\Delta y},
\end{aligned} \tag{A-9}$$

The notation $i^{\rightarrow}$ or $j^{\rightarrow}$ represents $i+\frac{1}{2}$, $j+\frac{1}{2}$, and the other superscript $\rightrightarrows$, $\leftarrow$ are the same as $+1$ and $-\frac{1}{2}$, respectively. To construct a complete PML system, one must set the proper damping coefficient. To compute the solution

inside the PML layers in the x-direction we used the same system of equations with $d^y = 0$, while for the PML layers in the y-direction we assumed $d^x = 0$. Figure A-2 presents the values of d^x and d^y for the different PML layers. The damping parameter can be written as $d(x) = d_0(x/\delta)^2$ in which δ is the length of the layer and d_0 is a function of the theoretical reflection coefficient $d_0 = \log(\frac{1}{R})\frac{3v_p}{2\delta}$. The stability condition used in the model of the wave propagation on a staggered grid was $\Delta t = 0.9\frac{h}{\sqrt{2}v_p}$ in which h denotes the grid size, which could be dx or dy.

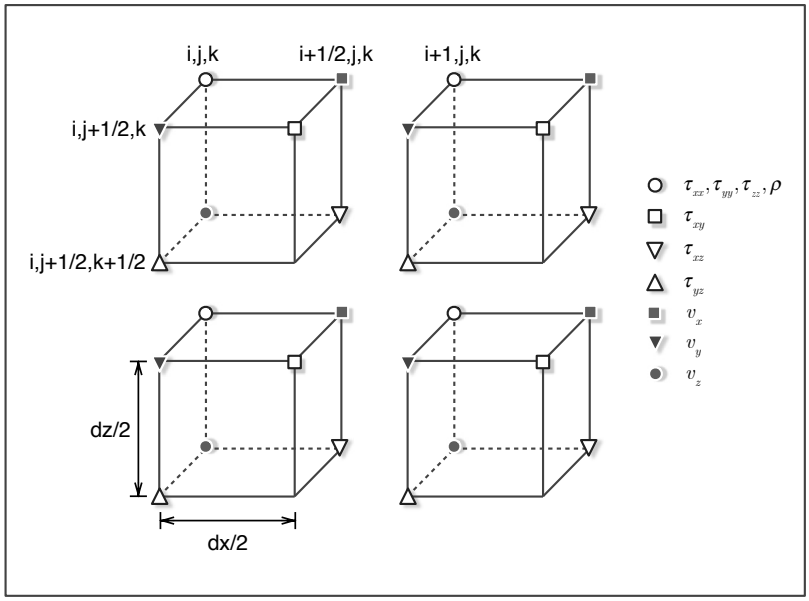

Figure A-1: The formulation of wave-propagation modeling in staggered grid. In this study, we concentrate on acoustic wave. Thus, we do not consider shear stress such as τ_{xy} or τ_{yz}.

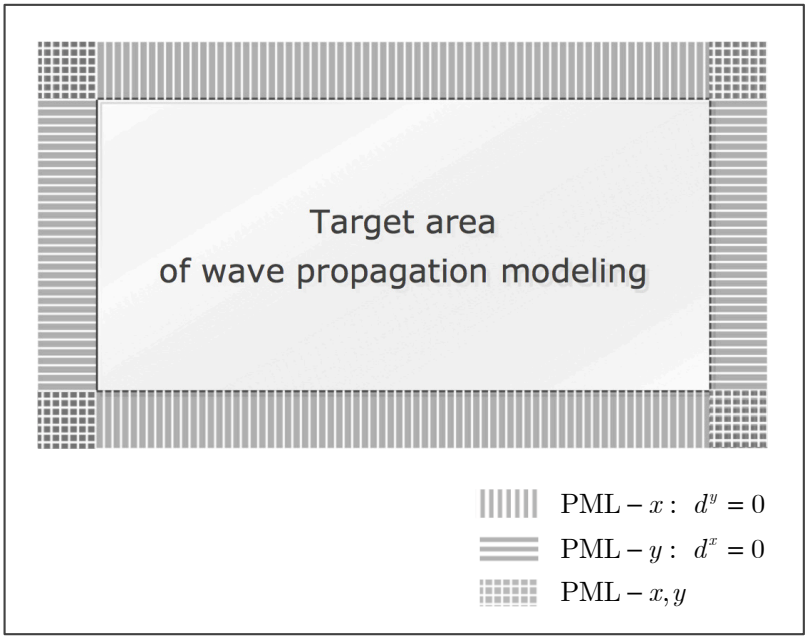

Figure A-2: PML boundary and the structure of damping coefficients corresponding to directions.

Bibliography

1. AMUNDSEN, L. Comparison of the leastsquares criterion and the cauchy criterion in frequency wavenumber inversion. *Geophysics 56* (1991), 2027–2035.

2. BISHOP, T. N., BUBE, K. P., CUTLER, R. T., LANGAN, R. T., LOVE, P. L., REASNICK, J. R., SHUEY, R. T., SPINDLER, D. A., AND WYLD, H. W. Tomographic determination of velocity and depth in laterally varying media. *Geophysics 50* (1985), 903–923.

3. BUBE, K., AND LANGAN, R. Hybrid l_1/l_2 minimization with applications to tomography. *Geophysics 62* (1997), 1183–1195.

4. CHIU, S. K. L., KANASEWICH, E. R., AND PHADKE, S. Three-dimensional etermination of structure and velocity by seismic tomography. *Geophysics 51* (1986), 1559–1571.

5. CHLIEH, M. Coseismic and afterslip of the great Mw 9.15 Sumatra-Andaman earthquake of 2004. *Bulletin of the Seismological Society of America 97* (2007), S152–S173.

6. CHOI, Y., SHIN, C., AND HEO, E. Efficient calculation method of the derivative of traveltime and amplitude using SWEET algorithm for refraction tomography. *Journal of Seismic Exploration 12* (2004), 327–341.

7. CLAERBOUT, J., AND GREEN, I. *Basic Earth Imaging*, madagascar ed. Staford Exploration Project.

8. CLAERBOUT, J., AND MUIR, F. Robust modeling with erratic data. *Geophysics 38* (1973), 826–844.

9. CLAYTON, R., AND ENGQUIST, B. Absorbing boundary conditions for acoustic and elastic wave equations. *Bulletin of the Seismological Society of America 67* (1977), 1529–1540.

10. DE AMORIM, W., HUBRAL, P., AND TYGEL, M. Computing field statics with the help of seismic tomography. *Geophysical Prospecting 35* (2012), 907–919.

11. ENGDAHL, E., VILLASENOR, A., DESHON, H., AND THURBER, C. Teleseismic relocation and assessment of seismicity (1918-2005) in the region of the 2004 Mw 9.0 Sumatra-Andaman and the 2005 Mw 8.6 Nias Island Great earthquakes. *Bulletin of the Seismological Society of America 97* (2007), S1–S19.

12. GRAINDORGE, D. Impact of lower plate structure on upper plate deformation at the NW Sumatran convergent margin from seafloor morphology. *Earth and Planetary Science Letters 275* (2008), 201–210.

13. GRAVES, W. Simulating seismic wave propagation in 3D elastic media using staggered-grid finite differences. *Bulletin of the Seismological Society of America 86* (1996), 1091–1106.

14. HA, T., CHUNG, W., AND SHIN, C. Waveform inversion using a back-propagation algorithm and a huber function norm. *Geophysics 74* (2009), R15–R24.

15. HA, W., CHUNG, W., AND SHIN, C. Pseudo-Hessian matrix for the logarithmic objective function in full waveform inversion. *Journal of Seismic Exploration 21* (2012), 201–214.

16. HA, W., PYUN, S., YOO, J., AND SHIN, C. Acoustic full waveform inversion of synthetic land and marine data in the Laplace domain. *Geophysical Prospecting 58* (2010), 1033–1047.

17. HENSTOCK, T., MCNEILL, L., AND TAPPIN, D. Seafloor morphology of the Sumatran subduction zone: Surface rupture during megathrust earthquakes? *Geology 34* (2006), 485–488.

18. HIGDON, R. Absorbing boundary-conditions for difference approximations to the multi dimensional wave equation. *Mathmatics of Computation 47* (1986), 437–459.

19. JANNANE, M., BEYDOUN, W., CRASE, E., CAO, D., AND KOREN, Z. Wavelengths of earth structures that can be resolved from seismic reflection data. *Geophysics 54* (1989), 906–910.

20. KOO, N., SHIN, C., MIN, D., PARK, K., AND LEE, H. Source estimation and direct wave reconstruction in Laplace-domain waveform inversion for deep-sea seismic data. *Geophysical Journal International 187* (2011), 861–870.

21. LAILLY, P. The seismic inverse probelm as a sequence of before stack migrations. In *Society for Industrial and Applied Mathmatics* (Philadelphia, USA, 1983).

22. MARFURT, K. Accuracy of finite-difference and finite-element modeling of the scalar and elastic wave-eqautions. *Geophysics 49* (1984), 533–549.

23. MARTIN, J., GHOSAL, D., AND SINGH, S. CHAUHAN, A. P. S. Downward continuation, tomography and pre-stack depth migration of streamer data. In *EAGE Abstract* (Copenhagen, Denmark, 1983).

24. MIN, D., AND SHIN, C. Refraction tomography using a backpropagation technique of waveform inversion. *Geophysics 71* (2006), R21–R30.

25. MORA, P. Nonlinear two-dimensional elastic inversion of multioffset seismic data. *Geophysics 52* (1987), 1211–1228.

26. MURPHY, G. E., AND GRAY, S. H. Manual seismic reflection tomography. *Geophysics 64* (1999), 1546–1552.

27. PLESSIX, R. A review of the adjoint-state method for computing the gradient of a functional with geophysical application. *Geophysical Journal International 167* (2006), 495–503.

28. PRATT, R., AND WORTHINGTON, M. The application of diffraction tomography to cross-hole seismic data. *Geophysics 53* (1988), 1284–1294.

29. PRATT, R., S. C., AND HICKS, G. Gauss-Newton and full Newton methods in frequency-space seismic waveform inversion. *Geophysical Journal International 133* (1998), 341–362.

30. PYUN, S., SHIN, C., AND SON, W. Frequency-domain waveform inversion using an l_1-*norm* objective function. In *EAGE Abstract* (Amsterdam, Netherlands, 2009).

31. RHIE, J., DREGER, D. BÜRGMANN, R., AND ROMANOWICZ, B. Slip of the 2004 Sumatra-Andaman earthquake from joint inversion of long-period global seimic waveforms and GPS static offsets. *Bulletin of the Seismological Society of America 97* (2007), S115–S127.

32. SHIN, C., AND CHA, Y. Waveform inversion in the Laplace domain. *Geophysical Journal International 173* (2008), 922–931.

33. SHIN, C., AND CHA, Y. Waveform inversion in the Laplace-Fourier domain. *Geophysical Journal International 177* (2009), 1067–1079.

34. SHIN, C., AND HA, W. A comparison between the behavior of objective functions for waveform inversion in the frequency and Laplace doamins. *Geophysics 73* (2008), VE119–VE133.

35. SHIN, C., KOO, N., CHA, Y., AND PARK, K. Sequentially ordered single-frequency 2D acoustic waveform inversion in the Laplace-Fourier domain. *Geophysical Journal International 181* (2010), 935–950.

36. SHIN, C., AND MIN, D. Waveform inversion using a logarithmic wavefield. *Geophysics 71* (2006), R31–R42.

37. SIBUET, J. 26th December 2004 Great Sumatra-Andaman Earthquake: seismogenic zone and active splay faults. *Earth and Planetary Science Letters 263* (2007), 88–103.

38. SYMES, W. Migration velocity analysis and waveform inversion. *Geophysical prospecting 56* (2008), 765–790.

39. TARANTOLA, A. Inversion of seismic-reflection data in the acoustic approximation. *Geophysics 49* (1984), 1259–1266.

40. YILMAZ, Ö. *Seismic data analysis*, volume 1 ed. Society of exploration geophysicists.

41. ZHANG, J., AND TOKSOZ, M. N. Nonlinear refraction traveltime tomography. *Geophysics 63* (1998), 1726–1737.

초 록

시뮬레이션을 통해 구한 파형과 관측 파형의 차이를 이용해 계산된 목적함수를 최소로 만드는 방향으로 지하 매질 변수를 갱신하여 지하 지질 구조를 계산해 내는 역산은 기존의 방식으로는 국부 최소값 문제, 저주파수 부재 문제와 잡음 문제 등 여러가지 요소로 인해 현장 자료에 적용하기에 어렵다. 이러한 문제점들을 보완하기 위해 라플라스-푸리에 영역 역산이 지하 매질 변수를 계산 해내기에 신뢰할 만한 도구로 알려져 있다. 라플라스 역산에서는 감쇄 파동장을 이용해 국부 최소값에 수렴할 가능성과 잡음에 대한 민감도를 낮추어 장파장 속도 모델을 구축한 후, 고주파수 성분을 이용해 실제 모델에 가까운 역산 결과를 얻는다. 그러나, 감쇄 파동장을 사용함으로 인해 깊은 영역에서 잔차와 기울기값이 불안정해진다. 따라서 영상화를 할 수 있는 깊이가 줄어들게 되며, 심해 탄성파 자료와 같이 영상화 깊이에 비해 오프셋의 거리가 짧을 경우 신뢰할 만한 결과를 얻기가 어렵다. 물층의 효과를 줄이기 위한 방법에는 탄성파 탐사를 수행할 때 긴 오프셋을 이용해 관측 자료를 얻는 방법과 하향 연속과 같은 수학적인 방법을 이용해 물층의 효과를 감소시키는 방법이 있다. 본 연구에서는 인공 합성 자료와 해양 탐사 현장 자료, 두 가지 경우에 대해 하향 연속을 적용하여 심부의 신호에 대한 신호와 굴절파에 대한 진폭을 강화시킨 파동장을 계산한 후, 이를 이용해 굴절파 토모그래피를 통해 장파장 속도 모델을 구성한 후에 이 결과를 초기모델로 하여 라플라스-푸리에 역산을 수행하였다. 역산 결과의 확인을 위해 계산된 속도 모델을 기초로 하여 역시간 구조 보정을 수행한 후, 역시간 구조 보정 결과로부터 공통 영상점(common-image gather)을 추출하여 이

를 기반으로 역산된 속도 모델의 타당성을 검증하였다.

주요어 : 라플라스-푸리에 영역 완전 파형역산, 하향연속, 굴절파 토모그래피, 심해 탄성파 자료

학번 : 2011-21111

Acknowledgement

본 논문을 쓰기까지 많은 분들의 도움이 있었습니다. 먼저 제게 많은 배움의 기회를 주신 신창수 교수님께 깊은 감사의 뜻을 전하고 싶습니다. 교수님 밑에서 생활하는 동안 꾸준함과 성실함을 배울 수 있었습니다. 또한, 무엇인가에 대해 항상 몰입하는 열정을 배웠습니다. 한 사람의 사회 구성원으로서 교수님의 깊은 가르침 잊지 않겠습니다. 또한, 바쁘신 와중에 논문 심사를 위해 시간을 내어주신 박형동 교수님과 민기복 교수님께도 감사드립니다.

이 주제로 연구가 시작될 수 있도록 도움을 주신 프랑스 파리 지구물리연구소의 Satish Singh 교수님, 최유진 박사님을 비롯한 연구원들께 감사의 마음을 전합니다. 파리에서 생활하는데 있어 어려움이 없도록 도와주신 Total 社의 Henri Calandra에게도 감사드립니다. 또, 연구실 생활을 하는 동안 바쁘신 와중에도 수 많은 도움을 주신 연구실의 기둥 하완수 박사님, 저의 멘토 김영서 박사님을 비롯한 연구실 동기와 선·후배님들께도 고마움을 전하고 싶습니다.

제가 지금까지 공부를 어려움 없이 할 수 있도록 지원을 아끼지 않으신 부모님께 가장 큰 고마움을 표합니다. 아직 부족한 점이 많지만 부모님께 남 부럽지 않은 아들이 되어가는 모습 보여드리겠습니다.

대학에 입학한지도 어느 덧 8년의 세월이 흘렀습니다. 8년의 생활을 함께한, 이제는 사회인이 된 05학번 동기들이게도 감사하며 사회 초년생인 친구들에게 이 기회를 빌어 응원의 힘을 실어주고 싶습니다. 고향을 떠나 타지 생활을 하는 동안 항상 서로에게 힘이 되어준 나의 오랜 벗, 장년에게도 이 기회를 빌어 고마움을 전하며, 앞으로도 끈끈한 우정 변치

않길 바랍니다.

본 논문은 MacTex을 기반으로 한 Texpad를 이용하여 작성되었으며, 국문 환경을 구축하기 위해 ko.Tex를 추가 활용하였습니다. 논문 작성을 위해 OmniGraffle pro., Seismic Un*x, Python, GPL library, Vim 등의 프로그램들을 사용하였습니다.